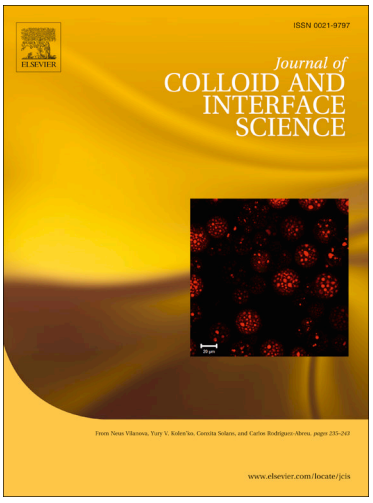

Solar light active silver/iron oxide/zinc oxide heterostructure for photodegradation of ciprofloxacin, transformation products and antibacterial activity

Amandeep Kaur, William A. Anderson, Shazia Tanvir, Sushil Kumar Kansal

PII: S0021-9797(19)31050-1
DOI: https://doi.org/10.1016/j.jcis.2019.09.017
Reference: YJCIS 25387

To appear in: *Journal of Colloid and Interface Science*

Received Date: 20 June 2019
Revised Date: 2 September 2019
Accepted Date: 4 September 2019

Please cite this article as: A. Kaur, W.A. Anderson, S. Tanvir, S. Kumar Kansal, Solar light active silver/iron oxide/zinc oxide heterostructure for photodegradation of ciprofloxacin, transformation products and antibacterial activity, *Journal of Colloid and Interface Science* (2019), doi: https://doi.org/10.1016/j.jcis.2019.09.017

Solar light active silver/iron oxide/zinc oxide heterostructure for photodegradation of ciprofloxacin, transformation products and antibacterial activity

Amandeep Kaur[1], William A. Anderson[2], Shazia Tanvir[2], Sushil Kumar Kansal[1]*

[1]Dr. S. S. Bhatnagar University Institute of Chemical Engineering and Technology, Panjab University, Chandigarh, 160014, India

[2]Department of Chemical Engineering, University of Waterloo, 200 University Avenue West, Waterloo, Ontario, N2L 3G1, Canada

Abstract

This paper reports on the multitasking potential of a silver/iron oxide/zinc oxide ($Ag/Fe_2O_3/ZnO$) heterostructure, which was used for the photocatalytic decomposition of ciprofloxacin (CPX) and bacterial disinfection. The $Ag/Fe_2O_3/ZnO$ heterostructure was successfully prepared using a facile precipitation method, and characterization results showed interesting structural, morphological, compositional and luminescent properties. The morphological results of the prepared heterostructure confirmed the deposition of Ag nanoparticles onto the surface of ZnO nanoplates and Fe_2O_3 nanorods. Treatment studies showed that the $Ag/Fe_2O_3/ZnO$ heterostructure had superior solar light driven photocatalytic activity towards CPX degradation(76.4%) compared to bare Fe_2O_3 nanorods (43.2%) and ZnO nanoplates (63.1%), Ag/Fe_2O_3 (28.2%) and Ag/ZnO (64.5%) under optimized conditions (initial CPX concentration: 10 mg/L; pH 4; catalyst loading: 0.3 g/L). Reactive species study confirmed the roles of e^-, h^+, $^{\bullet}OH$ and $^{\bullet}O_2^-$ in the photocatalytic degradation process. This photocatalytic behaviour of the $Ag/Fe_2O_3/ZnO$ heterostructure could be attributed to the improved full solar spectrum harvesting capacity, separation of charge carriers and migration of e^-/h^+ across the heterostructure interface. In addition, the $Ag/Fe_2O_3/ZnO$ heterostructure also showed good antibacterial activity against *Escherichia coli* (*E. coli*) under both dark and visible light conditions. This might be due to generation of reactive oxygen species during the reaction. To the best of our knowledge, this is the first study till date on the utilization of $Ag/Fe_2O_3/ZnO$ heterostructure for the photocatalytic degradation of CPX and *E. coli* bacteria disinfection. Therefore, this work offers an attractive path to design ZnO-based ternary heterostructures for solar-driven applications in wastewater remediation.

Keywords: $Ag/Fe_2O_3/ZnO$ heterostructure; catalytic performance, direct solar light; ciprofloxacin; antibacterial activity, *Escherichia coli*

*Corresponding Authors: sushilkk1@yahoo.co.in; sushilkk1@pu.ac.in,
Tel/Fax: +91-0172-2534920/+91-172-2779173

Highlights

- $Ag/Fe_2O_3/ZnO$ heterostructure was prepared *via* precipitation method.
- 76.4% CPX was degraded with $Ag/Fe_2O_3/ZnO$ after 210 minutes of solar illumination.
- CPX degradation largely succeeded by defluorination, hydroxylation and cleavage of piperazine ring.
- Heterostructure exhibited antibacterial characteristics against *Escherichia coli.*

1. Introduction

Fluoroquinolones have emerged as the third leading class of antibiotics and comprise around 17% of the worldwide antibiotics market [1]. Their presence in the aquatic environment has gained considerable attention due to their detrimental impacts on humans, animals and aquatic mammals through drinking water and food chain [2]. Ciprofloxacin (CPX), a second-generation fluoroquinolone, has been most widely prescribed for the treatment of anthrax, tuberculosis, bladder infection, sexually communicable diseases and problems related to the gastrointestinal tract because of its broad range of antibacterial activity [1, 3-5]. It enters the aquatic environment such as wastewater, ground water, surface water and even in drinking water *via* runoff, un-metabolized excretion (>75% of administrated CPX) and inappropriate disposal of unused and expired drugs [6-10]. Drug manufacturing companies account for up to 31000-50000 µg/L in sewage water while approximate concentrations of CPX in wastewater treatment plants is in the range of 209-405 ng/L [11, 12]. CPX has been regarded as amongst the top ten priority pharmaceutical drugs that are found in the water cycle and is a major target compound of concern for European Union projects [13, 14]. It has a stable nature and can propagate bacterial drug resistance even in minute concentrations, leading to significant concerns for human health and ecosystems [15]. The negative impacts of CPX on living creatures involve antibiotic resistance in bacteria, particularly in *Escherichia coli* (*E. coli*) [16]. Moreover, several reports confirm the presence of CPX residues in fish tissues because of the bio-accumulation tendencies of CPX [17, 18]. Thus, the removal of CPX from the aquatic environment has already become a matter of concern because of its ecotoxicological effects

and ability to encourage resistance in bacterial species [19]. There is an urgent need to develop effective treatment techniques for eliminating these drugs from the aqueous phase.

Semiconductor mediated heterogeneous photocatalysis is considered to be a green and sustainable technology for addressing some environmental pollution, and it has received much attention owing to its promising prospects in wastewater treatment using solar energy [20-24]. Numerous wide band gap semiconductors such as TiO_2, ZnO, SnO_2 and WO_3 photocatalysts have gained significant research investigation globally [25-27]. Among these well-known metal oxides, ZnO, a group II-VI semiconducting material has been broadly employed in the field of gas and chemical sensing, solar cells, photodetectors, optoelectronic and catalysis owing to its exceptional piezoelectrical, optical and magnetic properties [28-30]. The outstanding features of ZnO include non-toxicity, cost effectiveness and easy fabrication into different morphologies, and these features make it suitable for a variety of applications. However, there are certain photochemical shortcomings associated with this semiconductor such as a low quantum efficiency, photo-corrosion and restricted light absorption capacity due to the rapid recombination of photo-induced charge carriers [31]. Thus, recent research has been concentrated on overcoming these limitations through doping with noble and transition metals, introduction of two or more metals ions as co-dopants, formation of heterostructures by combining with other band gap materials (*for instance*, Cu_2O, WO_3, CdS and Fe_2O_3) and by controlling the growth of ZnO materials in terms of shape, size and structure.

Hematite (α-Fe_2O_3) is mainly recognized as a capable visible light driven photocatalyst owing to its availability, non-toxicity and suitable band potential positions for redox reactions [32-34]. In addition, α-Fe_2O_3 is the highly thermodynamically-stable form of an n-type semiconducting iron oxide with a band gap of about 2.2 eV, and it has been extensively studied for prospective applications in gas sensing, batteries, heterogeneous catalysis and environmental purification [35-40]. Moreover, Fe_2O_3 nanoparticles have already been employed for food and medical purposes as approved by the FDA in the United States [41]. It has been gradually utilized in the field of photocatalysis because of its high absorption capacity in the visible region, which is around 43% of the full solar spectrum [42]. Unfortunately, a higher rate of recombination of photo-induced charge carriers has inhibited further growth and practical applications of α-Fe_2O_3 as an effective photocatalyst. Therefore, many researchers have fabricated heterostructures by uniting the merits of both Fe_2O_3 and ZnO, which has offered exceptional properties in the area of photocatalysis [43]. Xie *et al.*[44] reported the synthesis of α-Fe_2O_3/ZnO composite and carried out the effective photocatalytic

decomposition of pentachlorophenol under UV light. Another study reported the degradation of methyl orange over a spindle shaped α-Fe_2O_3/ZnO composite under ultraviolet light. The prepared composite achieved 70% decomposition of methyl orange under solar illumination which was 3.5 times more than bare Fe_2O_3 [45]. Alternatively, the combination of heterostructures with noble metal nanoparticles such as Cu, Co, Ag and Au *etc.* is a possible strategy that not only enhances the photocatalytic efficiency but also has a substantial effect on the morphology [46-48]. Furthermore, surface modification with Ag nanoparticles could improve the separation of photo-generated charge carriers owing to its outstanding conductivity and strong electron capturing ability [49].

Municipal wastewater also contains different species of bacteria, other microbes, and pathogens which should be monitored and controlled during wastewater remediation [50-52]. In most cases, water and wastewater treatment criterion focus only on coliform organisms including *E. coli*. [53]. *E. coli* is a potentially pathogenic organism and exists in the aquatic environment which can cause waterborne diseases like diarrhoea, cystitis and peritonitis.[54, 55]. Its presence in the aquatic environment can disturb ecological balance and poses a threat to human health even at smaller concentrations [56, 57]. About two million people are killed every year through bacterial infections throughout the world [58]. Therefore, the advancement of nanomaterials with antibacterial properties is also of considerable interest. Various metal oxides such as TiO_2, ZnO, CuO and Fe_2O_3 are well known for effective inactivation of bacteria using photocatalyzed chemical reactions [59-62], however research in the area of hybrid-metal oxides still requires broad exploration. Tam *et al.* [64] prepared ZnO rods using a hydrothermal method and these exhibited a higher antibacterial activity against *Bacillus atrophaeus* as compared to *Escherichia coli* owing to its simple cell structure. Another study reported the photocatalytic decomposition of orange II dye and *E.coli* disinfection over ZnO under solar light [64]. However, there are no reports available in literature on the photocatalytic and antibacterial activity of a heterostructure like Ag/Fe_2O_3/ZnO.

With reference to the above considerations, the motive of this study was to fabricate Ag/Fe_2O_3/ZnO heterostructures through a simple precipitation technique and to characterize them using several analytical and spectrometric techniques. The prepared heterostructure was employed for the decomposition of an antibiotic drug, CPX, under natural solar illumination as well as to assess its antibacterial activity against *E. coli* under dark and light conditions. The prepared Ag/Fe_2O_3/ZnO heterostructure exhibited higher photocatalytic activity for the degradation of CPX than bare ZnO. Moreover, the function of reactive species in the

photocatalytic decomposition of ciprofloxacin and the antibacterial experiments was assessed through studies with radical scavengers. The probable photocatalytic mechanism of the as-prepared $Ag/Fe_2O_3/ZnO$ heterostructure was explored, followed by an assessment of its reusability.

2. Materials and Methods

2.1. Chemicals and reagents

All the analytical grade chemicals were used as supplied. Zinc acetate dihydrate ($(CH_3COO)_2Zn.2H_2O$; ≥ 98%), iron (III) nitrate nonahydrate ($Fe(NO_3)_3.9H_2O$; ≥ 97%), sodium hydroxide (NaOH; > 97%), hydrochloric acid (HCl; 36.5-38%), silver nitrate ($AgNO_3$; ≥ 99%), triethanolamine (TEOA; ≥ 97%), formic acid (FA; > 98%), *p*-benzoquinone (*p*-BQ; ≥ 98%) and sodium sulfate anhydrous ($(Na_2SO_4$; ≥ 99%) were procured from Merck, India. Ethanol (C_2H_5OH; > 99.9%) was purchased from Merck KGaA, Germany. Ethylenediamine tetraaceticacid disodium salt (EDTA.2Na; > 99.4%) and glutathione (GSH; > 98%) were purchased from Alfa Aesar and Sigma Aldrich Canada, respectively. Ciprofloxacin (CPX; ≥ 98%), terephthalic acid (TA; 98%) and sodium carbonate ((CNa_2O_3); ≥ 99.5%) were purchased from Sigma Aldrich, USA. Sodium nitrate ($NaNO_3$; 98%) was procured from Fisher Scientific, India. Double distilled water was used to prepare stock solutions for all experiments. The adjustment of the pH of drug solutions was performed with 0.01 M solutions of HCl and NaOH.

2.2. Preparation of Fe_2O_3 nanopowder

In the typical synthesis procedure, 3.6 g of $Fe(NO_3)_3.9H_2O$ was dispersed in 40 mL double distilled water under continuous stirring. After that 3M NaOH was added to the precursor solution until the pH reached 11. Further, this solution was given ultrasonic treatment for 10 minutes and stirring for 1hour. Afterwards, the whole suspension was poured into a Teflon-lined stainless steel autoclave and treated hydrothermally at 150°C for 14 hours. The obtained precipitates were centrifuged, collected and washed with ethanol and double distilled water and dried in an oven at 80°C. Subsequently, the resulting yellow powder was calcined at 450°C for 2 hours.

2.3. Preparation of $Ag/Fe_2O_3/ZnO$ heterostructure

The $Ag/Fe_2O_3/ZnO$ heterostructure was synthesized *via* an ultrasonic-assisted hydrothermal method. In this method, 0.5 g Fe_2O_3 was suspended in 25 mL of distilled water

under ultrasonication to form "Solution A". Simultaneously, 2.748 g of zinc acetate dihydrate and 0.094 g of silver nitrate was dissolved into 20 mL and 10 mL distilled water, respectively and mixed thoroughly. Afterwards, 1 M NaOH was added into aqueous solution to achieve pH of 12 and this was designated as "Solution B". Both solutions A and B were mixed and stirred for 1 h. The whole mixture was then transferred into the Teflon-lined autoclave and hydrothermally treated at 150 °C for 10 h. The collected precipitates were washed carefully with an ethanol-water mixture, dried at 70°C overnight in an oven, and then crushed into powder form and further calcined at 450°C for 2 h. The pure ZnO, was synthesized using the same method, except for the inclusion of silver nitrate and Fe_2O_3. The Ag/Fe_2O_3 and Ag/ZnO samples were also prepared using same procedure without the addition of zinc acetate dihydrate and Fe_2O_3, respectively.

2.4. Analytical methods

The general morphologies and structure of as-prepared materials were investigated *via* transmission electron microscopy (TEM; JEOL-JEM-2100F) and field emission scanning electron microscopy (FESEM; HITACHI, SU8010) equipped with an energy dispersive spectroscope (EDS) at an accelerating voltage of 10 kV. The interaction between the heterostructure and *E. coli* was captured using a Philips CM10 microscope. The structure and crystalline properties of samples were obtained with X-ray diffraction (XRD; PANanalyticalXpert Pro.), measured with Cu-Kα (λ= 1.54056 Å) at 45 kV and 40 mA. The presence of surface functional groups was assessed using Fourier transform infrared (FTIR) spectrophotometer (Perkin Elmer spectrum 400-FTIR/FT-FIR) using KBr as a standard material. The elemental composition and state of prepared samples was confirmed using an X-ray photoelectron spectrophotometer (Thermal Scientific K-alpha).The specific surface area and pore volume were determined using nitrogen adsorption analyzer (NOVA 2000e series, Quantachrome Instruments).The ultraviolet–visible diffuse reflectance spectra of samples were acquired on UV–vis DRS (Shimadzu UV-2600) using barium sulphate as a reference material. Photoluminescence (PL) spectra of samples were collected using fluorescence spectrophotometer (Hitachi F-7000; 5J1-004 model). The UV–vis absorption studies were carried out by recording absorbance spectra on Systronics-2202 spectrophotometer. The zeta potential of prepared catalyst at different pH values was determined using zetasizer (Nano-ZS90, Malvern Instruments Ltd, UK). The valence band potentials of prepared samples were determined using ultraviolet photoelectron spectroscopy (UPS, AXIS Supra, Kratos Analytical, UK).The reaction transformation products for the decomposition of CPX over $Ag/Fe_2O_3/ZnO$

heterostructure was analyzed using ultra performance liquid chromatography (UPLC) with a Waters mass spectrometer (XEVO G2XS QTOF) for analysis of the mass spectra. The separation was carried out in an Acquity BEH C18 column (2.1* 100 mm i.d., 1.7 μm). Chromatographic separation was carried out with a mobile phase containing 0.1% formic acid in deionised water and 100% acetonitrile passed through the column with a sample injection volume of 1 μL and syringe pump flow rate of 0.3 mL/min. The positive electron ionization mode was used to obtain the mass spectra with scanning range of 100-1000 m/z under the following conditions: capillary voltage 2.5 kV; cone voltage 30V; source temperature 120°C; desolvation temperature 400 °C.

2.5. Photocatalytic measurements

The extent of photocatalytic activity of $Ag/Fe_2O_3/ZnO$ heterostructures was examined by monitoring the decomposition of CPX in a double wall reaction vessel covered with parafilm under solar illumination between 10:30 am to 2:30 pm with average intensities of 65-70 Klux measured using a CHY-332 digital light meter (Longitude 76^0 46' 14" E and Latitude 30^0 45' 34" N). Briefly, a certain amount of photocatalyst, *i.e.* $Ag/Fe_2O_3/ZnO$ with a dose varying from 0.1 g/L to 0.4 g/L, was suspended in 100 mL of CPX (10 mg/L) aqueous solution. Prior to illumination, the suspension was stirred in the dark for 30 minutes to attain adsorption-desorption equilibrium. Subsequently, the investigation of photocatalytic activity was commenced by irradiating the set up under solar light. Samples of CPX solution were extracted at specific time spans and filtered to obtain a photocatalyst-free drug solution. The concentration of CPX solution was determined at an absorption wavelength of 270 nm using Systronics-2202 UV-vis spectrophotometer. The process parameters (pH of drug solution, catalyst dose and initial CPX concentration) were examined by varying the reaction conditions. The degradation extent (%) was calculated by formula given below:

$$\text{Degradation extent (\%)} = \frac{C_o - C_t}{C_o} \times 100$$

where C_0 is the concentration of CPX before solar illumination and C_t is the concentration of CPX at time t of solar light illumination.

Furthermore, scavenger experiments were performed to determine the reactive species accountable for degradation, using distinct scavengers such as formic acid (FA; HCOOH), triethanolamine (TA; $C_6H_{15}NO_3$) and *p*-benzoquinone (*p*-BQ; $C_6H_4O_2$) for trapping of e^-, h^+ and $^{\bullet}O_2^-$, respectively. Before the addition of photocatalyst, scavengers (0.01 M) were added into the CPX solution, and the previously described solar procedure was followed.

2.6. Assay for antibacterial activity measurements

$Ag/Fe_2O_3/ZnO$ heterostructure suspensions were sterilised and investigated for their antibacterial activity toward the Gram-negative bacteria *E. coli,* which was grown for 17 h in Lauryl Tryptose broth (LTB) in an incubator shaker with a shaking speed of 150 rpm at 37°C. After incubation, bacterial suspension was centrifuged in 1.5 mL tube and the bacterial pellet was recovered by discarding the supernatant. The obtained pellet was washed three times with 10 mM phosphate buffered saline (PBS). Then, this washed pellet was re-suspended in PBS and the optical density of this stock solution of bacteria was adjusted to 0.2 at 600 nm using PBS. The bacterial concentration was also confirmed by plate counting of serial dilutions and the initial concentration was found to be approximately 3×10^7 colony forming units per millilitre **(**CFU/mL). All glassware and microtips were sterilized by autoclave prior to each experiment.

Different concentrations of $Ag/Fe_2O_3/ZnO$ heterostructure (0-2000 μg/mL) were prepared in sterile deionised water. Then, 900 μL of the samples containing different concentrations of $Ag/Fe_2O_3/ZnO$ heterostructure was added to 100 μL of inoculum of *E.coli* (3×10^7 CFU/mL). The prepared suspensions were incubated on a shaker at 37°C with a rotational speed of 150 rpm for incubation times of 30, 60 and 120 minutes under dark and visible light conditions (fluorescent lamps model F328/XL/SPX35/HL/ECO (430-630 nm; 2915 lumens). After the specified exposure time, a sample was serially diluted and 100μL was added to plate count agar plates and spread homogenously over the plate with help of a sterile spreader. The plates were incubated at 37°C for 24 h, and the numbers of bacteria colonies were counted. Control experiments were carried out in the same manner without the addition of $Ag/Fe_2O_3/ZnO$ heterostructure.

3. Results and discussion

3.1 Characterization of prepared $Ag/Fe_2O_3/ZnO$ sample

The phase and structural properties of as-prepared ZnO and $Ag/Fe_2O_3/ZnO$ were investigated by XRD analysis (**Figure 1**a). The diffraction peaks obtained at 2θ = 31.85°, 34.62°, 36.37°, 47.63°, 56.56°, 62.85°, 66.51°, 68.01°, 69.15°and 77.01°corresponded to (100), (002), (101), (102), (110), (103), (200), (112), (201) and (202) lattice planes of the standard pattern of the wurtzite hexagonal phase of ZnO (JCPDS 36-1451), respectively [65, 66]. Further, the average crystallite size (D) of the prepared ZnO was computed at peak (101) using

Debye- Scherrer equation and calculated to be 41.7 nm. **Figure 1**b represents the XRD pattern of the prepared Fe_2O_3 and it possessed a rhombohedral structure along with space group of R-3c. The diffraction peaks observed at 2θ = 24.28°, 33.28°, 35.75°, 40.97°, 49.53°, 54.16°, 57.52°, 62.57°, 64.12° and 71.82° corresponded to (012), (104), (110), (113), (024), (116), (122), (214), (300) and (1010) planes of α-Fe_2O_3 (JPCDS No. 33-0664), respectively [67-69] and the crystallite size at plane (110) was determined to be 21.57 nm. In addition, two diffraction peaks at 38.01° and 44.15°were related to (111) and (200) planes of Ag, respectively [70], confirming the formation of a ternary composite Ag/Fe_2O_3/ZnO (**Figure 1**c). The crystallite size (D) of ZnO (101) of the prepared Ag/Fe_2O_3/ZnO heterostructure was computed from the Debye-Scherrer equation and calculated to be ~100 nm. As shown in **Figure 1**d and e, the XRD patterns of the as-prepared Ag/Fe_2O_3 and Ag/ZnO nanocomposites contain the peaks of both Ag, α-Fe_2O_3 and Ag, ZnO, respectively. Other than the composites, no diffraction peak associated with another crystal phase was observed, confirming the high purity of the synthesized samples.

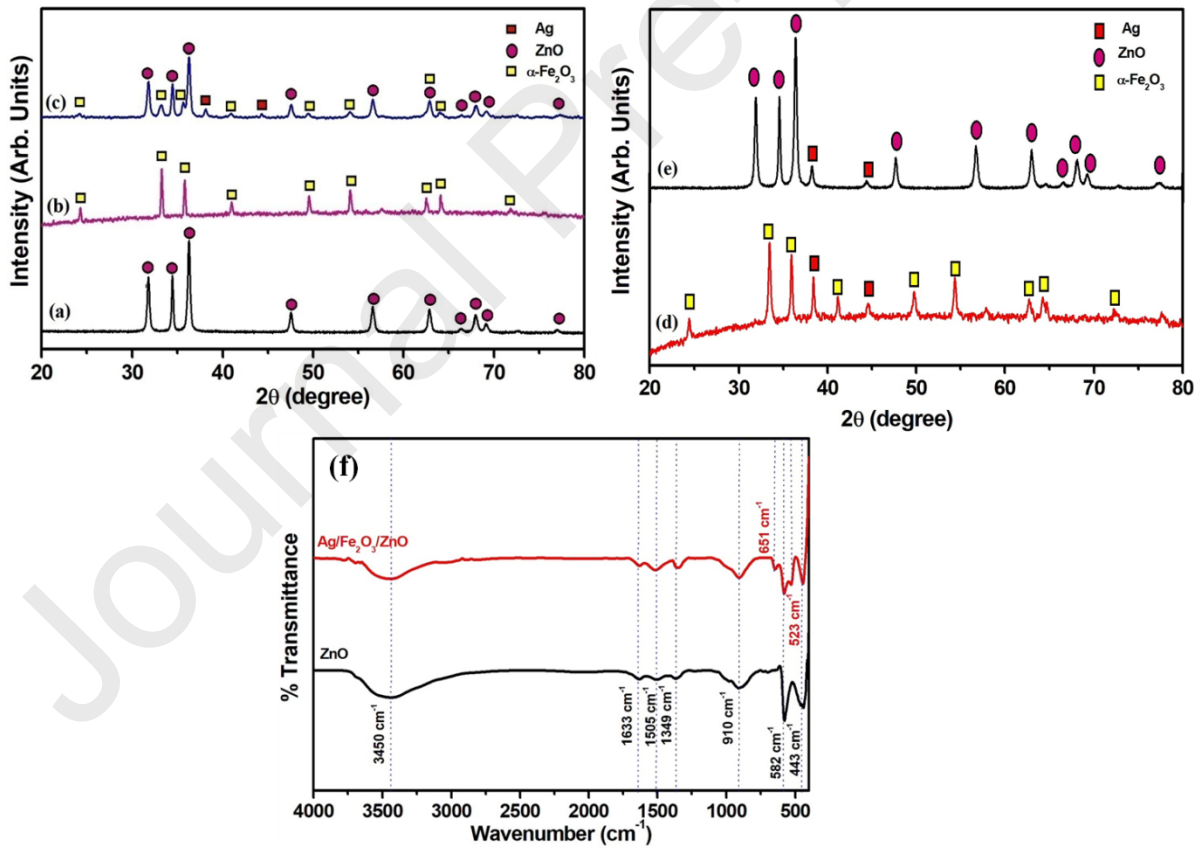

Figure 1. XRD diffraction patterns of (a) bare ZnO, (b) bare Fe_2O_3 (c) Ag/Fe_2O_3/ZnO heterostructure (d) Ag/Fe_2O_3 (e) Ag/ZnO and (f) FTIR spectra of ZnO and Ag/Fe_2O_3/ZnO

Information regarding the surface chemistry of the prepared samples was obtained from FTIR patterns (**Figure 1**f). From the spectrum of pure ZnO, the characteristic bands at 443 cm^{-1} and 582 cm^{-1} corresponded to the stretching vibrations of oxygen-metal-oxygen (O-M-O) and metal-oxygen (M-O), respectively [71]. Notably, two extra peaks were obtained in the prepared heterostructure at 523 cm^{-1} and 651 cm^{-1}, which corresponded to metal-oxide (Fe-O) vibrations [72]. A peak observed at 910 cm^{-1}can be due to the bending modes of a carbonate group [73]. A small band at 1349cm^{-1} represents C-H bending [74]. The peak at 1505 cm^{-1}corresponds to symmetrical vibrations of a C=O group [75]. The band at 1633 cm^{-1} and 3450 cm^{-1} is attributed to the bending and stretching vibrations of an O-H group [76, 77].

The morphology and structure of as-synthesized Ag/Fe_2O_3/ZnO heterostructure, bare ZnO and α-$Fe_2O_3$was studied using FESEM analysis. **Figure 2**a and b indicate that the pure ZnO sample is composed of many nanosheets with a thickness of 20-50 nm. These nanosheets are highly aggregated and grown in more dense form. It can be seen that the α-Fe_2O_3 material shows a rod-like structure (**Figure 2**c and d)) with a diameter of 30-100 nm and length in the range of 0.4-0.65µm.

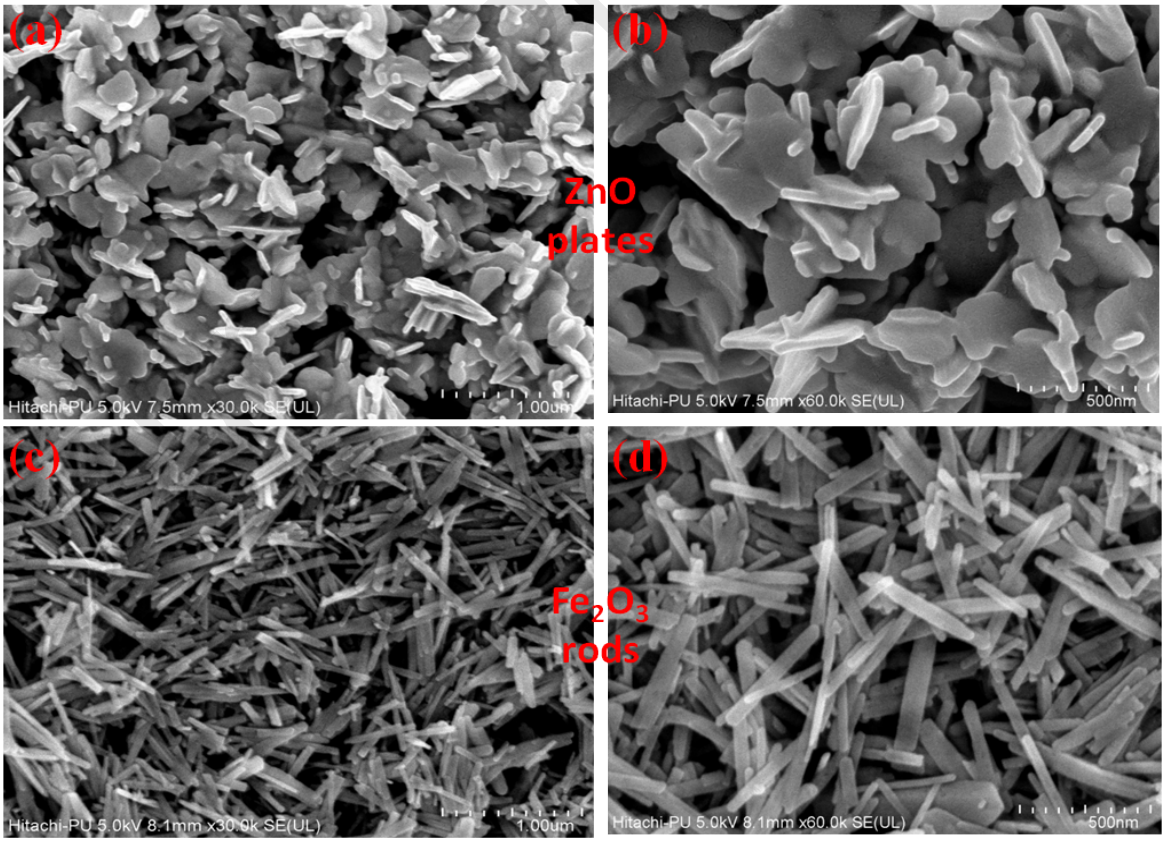

Figure 2. FESEM images of (a), (b) ZnO at different magnification, (c) and (d) Fe_2O_3 at different magnifications

Figure 3(a-c) shows FESEM micrographs of the synthesized Ag/Fe_2O_3/ZnO heterostructure. A high resolution FESEM micrograph (**Figure 3**b) indicates that ZnO nanoplates and α-Fe_2O_3 nanorods are assembled to form a heterostructure, while Ag nanoparticles are non-uniformly distributed on the surface of this heterostructure. **Figure 3**d and **3**e exhibit the TEM images of the as prepared heterostructure which confirmed the obtained FESEM results with respect to the structure and dimensions of the prepared sample. In order to verify the crystalline phases which were identified *via* XRD analysis using interplanar spacing, an HRTEM investigation was carried out on the prepared Ag/Fe_2O_3/ZnO sample. The different lattice fringes (**Fig 3**f) noted at 0.25 nm and 0.27 nm are consistent with ZnO (101) and the hexagonal phase of α-Fe_2O_3 (104) facets respectively [78-80]. The lattice fringe was measured to be 0.24 nm and this corresponded to the (111) plane of the cubic phase of Ag [81-82]. In addition, element mapping (**Figure 3**(g-j)) of selected areas showed the uniform interspersion between the Ag, Fe_2O_3 nanorods and ZnO sheets. The EDS analysis (**Figure 3**k) of the ternary Ag/Fe_2O_3/ZnO heterostructure also validated the existence and weight percentage of the relative components (Zn, Fe, O and Ag) in the heterostructure.

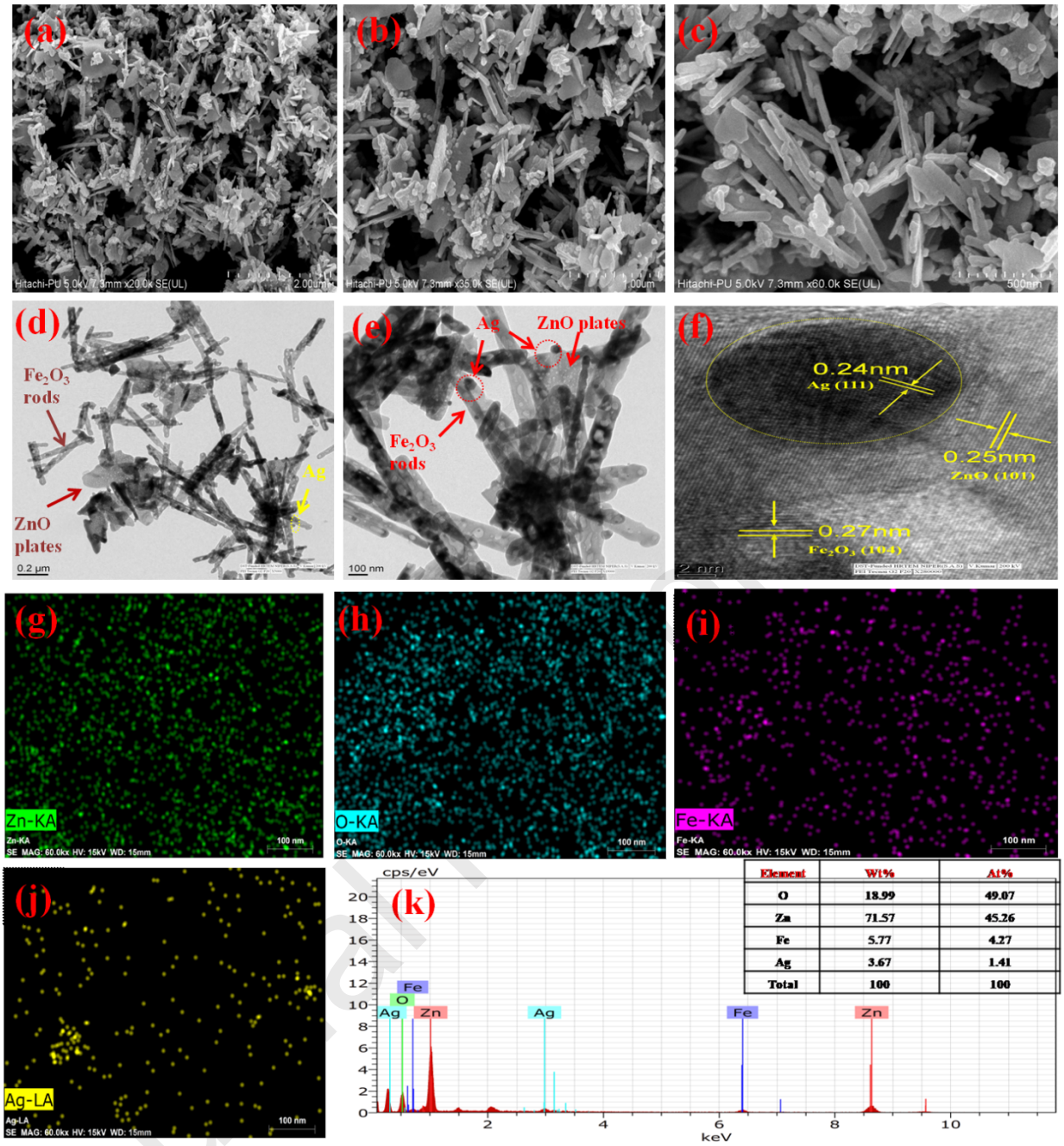

Figure 3.(a-c) FESEM micrographs, (d-e) TEM images at different magnifications, (f) HRTEM image, (g-j) Element mapping; Zn, O, Fe, Ag and (k) EDS analysis of prepared $Ag/Fe_2O_3/ZnO$ heterostructure

XPS analysis was carried out to investigate the elemental composition and electronic state of the $Ag/Fe_2O_3/ZnO$ heterostructure (**Figure 4**). **Figure 4**a exemplifies the XPS survey spectrum of the prepared heterostructure, which confirmed that the sample $Ag/Fe_2O_3/ZnO$ heterostructure was comprised of Ag, Zn, Fe and O elements, as found in the aforementioned TEM, EDX and XRD results. **Figure 4**(b-e) displays the high-resolution spectrum for Zn, Fe,

Ag and O elements. Because of high spin-orbit pairing, the Zn 2p peak breaks up into Zn $2p_{3/2}$ and Zn $2p_{1/2}$ peaks centred at 1021.3 eV and 1044.3 eV, respectively. Results showed that the chemical state of Zn remains the same i.e. Zn^{2+} in the composite [83, 84]. As illustrated in **Figure 4**c, for the Fe 2p XPS spectrogram, two peaks located at binding energy positions of 710.3 eV, 723.8 eV can be ascribed to Fe $2p_{3/2}$ and Fe $2p_{1/2}$, respectively [85]. The small peak positioned at 718.3 eV is associated with a satellite peak of Fe $2p_{3/2}$. Another lower intensity peak at 732.6 eV may be related to a satellite peak of Fe $2p_{1/2}$ [86]. These satellite peaks confirm the presence of Fe^{3+} in the hematite phase of Fe_2O_3 and indicate that Fe^{2+} is missing [87, 88]. In **Figure 4**d, the peaks obtained at 368.4 eV and 374.5 eV corresponded to Ag $3d_{5/2}$ and Ag $3d_{3/2}$ respectively, which confirms the presence of Ag^0 on the surface of the prepared composite [73, 83, 89-90]. The peaks related to Ag^+ cations were not obtained in the XPS spectrogram. The peak located at 531.5 eV (**Figure 4**e) is attributed to the adsorbed oxygen molecule on the surface of $Ag/Fe_2O_3/ZnO$ heterostructure [91].

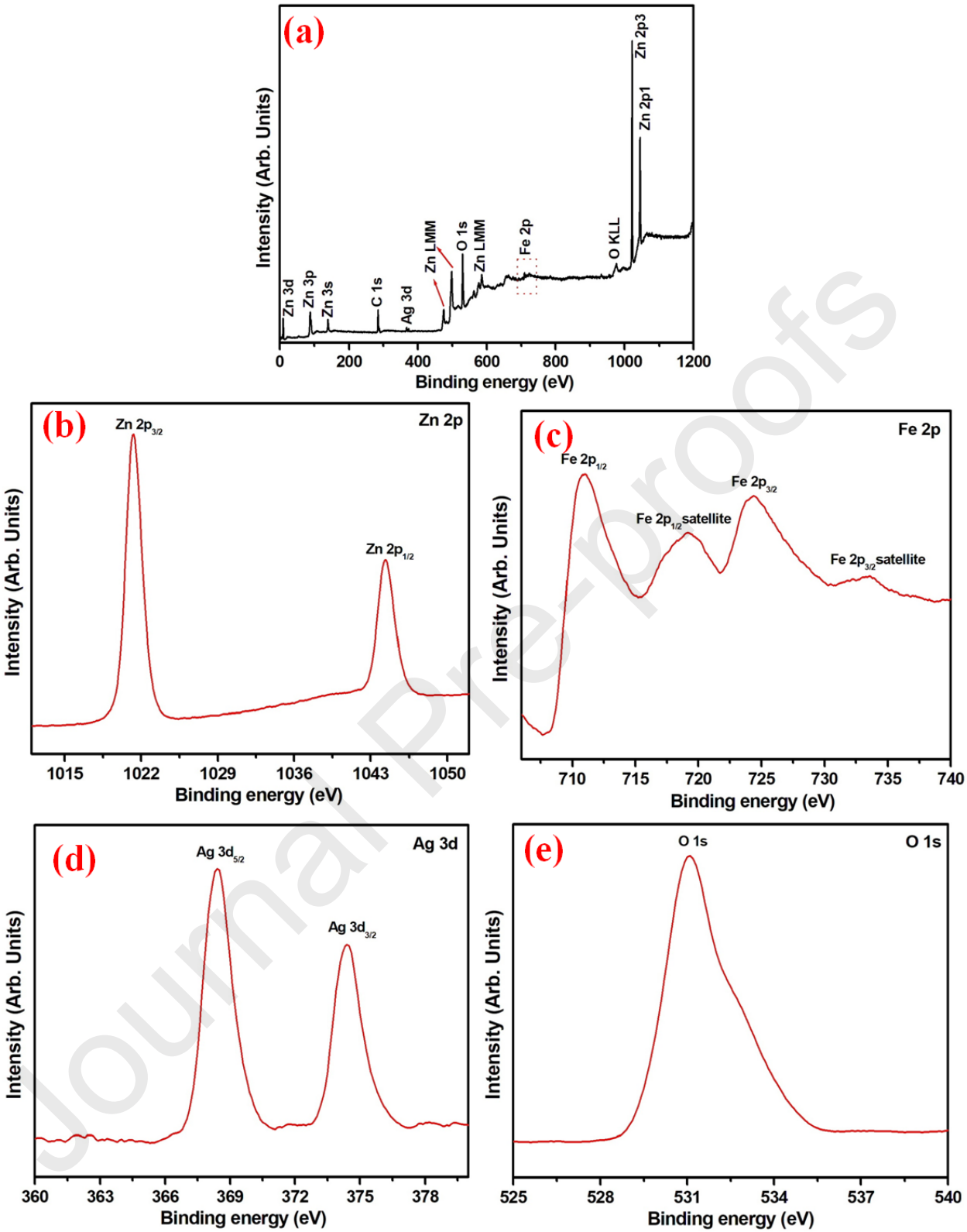

Figure 4. (a) XPS spectra of the Ag/Fe_2O_3/ZnO heterostructure, (a) survey scan, (b) Zn 2p, (c) Fe 2p, (d) Ag 3d and (e) O 1s

The optical absorption characteristics of the prepared samples are related to electronic arrangements, which play a crucial role in determining its photocatalytic activity [92]. The energy band gaps (E_g) were calculated from the plot of $(\alpha h\nu)^2$ versus $h\nu$ (**Figure 5**a). The energy band gap was determined by drawing a linear slope according to the following empirical formula:

$$(\alpha h\nu)^n = A\,(h\nu - E_g)$$

where α, $h\nu$, E_g, A corresponded to the coefficient of absorption, photonic energy, band gap energy and proportionality constant, respectively. The value of n is dependent on the direct optical transmission of the material and was assumed to be 2. The band gap of the prepared samples was found to be 3.18 eV, 2.93 eV and 2.07 eV for ZnO nanoplates, $Ag/Fe_2O_3/ZnO$ heterostructure and Fe_2O_3 nanorods, respectively. Hence, it can be deduced that the inclusion of Ag/Fe_2O_3 into ZnO nanoplates can improve the light absorption and catalytic activity for the removal of organic contaminants under the full solar spectrum [93]. The improved light absorbing capacity of the ternary composite makes it appropriate for solar light-based applications.

The Photoluminescence (PL) technique was used to study the transfer, capture and separation of photo-induced electron hole pairs in prepared catalysts. PL spectrograms of the prepared $Ag/Fe_2O_3/ZnO$ heterostructure and pristine ZnO nanoplates are shown in **Figure 5**b. They both follow similar trends but distinct PL intensities, which confirm the existence of ZnO matrix in the prepared $Ag/Fe_2O_3/ZnO$ heterostructure. The emission spectra for the $Ag/Fe_2O_3/ZnO$ heterostructure and the ZnO nanoplates were recorded by exciting both samples at the 325 nm wavelength. The emission peaks formed at 403 nm and 471 nm can be attributed to zinc vacancies and interface radiation imperfections, respectively [94, 95]. Moreover, the blue emission range (470-550 nm) was generally related to oxygen interstitials [96]. The $Ag/Fe_2O_3/ZnO$ heterostructure exhibited significantly decreased PL intensity as compared to bare ZnO nanoplates, indicating that the recombination rate of photoexcited e^--h^+ pairs can be effectively inhibited and therefore extending the lifespan of charge carriers. This behaviour can be a favourable factor for enhancing its photocatalytic properties.

The large specific surface area of the composite offers more availability of active sites, improves the charge movement and thereby can be responsible for enhanced photocatalytic activity [97]. **Figure 5**c and d exhibits the nitrogen adsorption-desorption isotherm and pore size distribution curve of the prepared $Ag/Fe_2O_3/ZnO$ heterostructure. The specific surface area

and pore volume for the $Ag/Fe_2O_3/ZnO$ heterostructure was determined to be 33.440 m^2/g and 0.038 cm^3/g, respectively. The DFT distribution plot exhibited in **Figure 5**d shows that the pore radius distribution peak was centred at 13.59 Å.

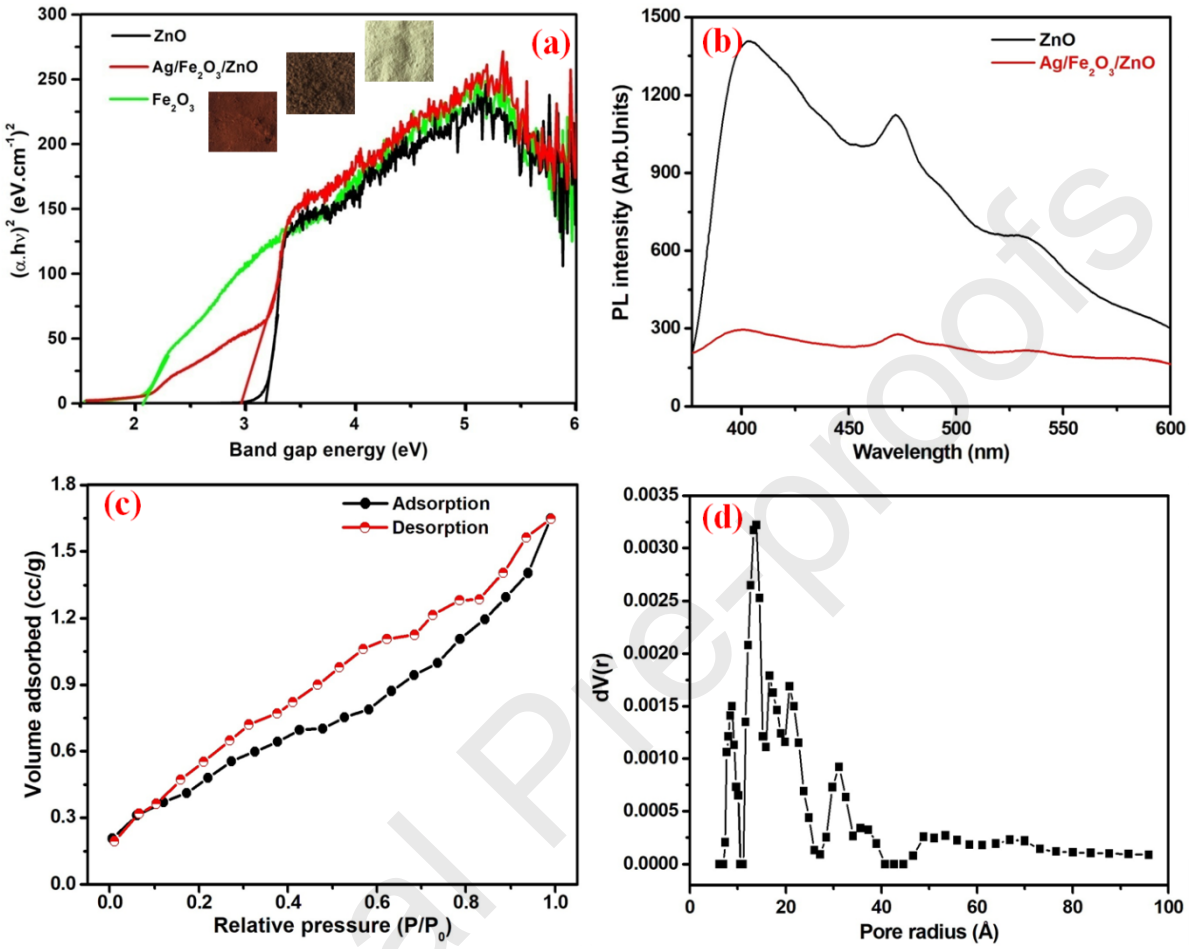

Figure 5. (a) Plot of $(\alpha h\nu)^2$ versus hν(b) photoluminescence spectra at 325 nm excitation (c) BET adsorption-desorption isotherm and (d) Density functional theory (DFT) analysis of as-prepared $Ag/Fe_2O_3/ZnO$

3.2 Photocatalytic decomposition of CPX over $Ag/Fe_2O_3/ZnO$ heterostructure under solar illumination

The photocatalytic activity of the prepared materials was investigated by the decomposition of CPX under different conditions. The effects of various parameters such as initial pH, $Ag/Fe_2O_3/ZnO$ loading, and initial CPX concentration were investigated. Moreover, photocatalyst reuse experiments were carried out to examine the performance of the prepared material for realistic purposes.

The solution pH plays very complex role in a photocatalytic decomposition system. It affects various factors such as the ionization state of the substrate and the surface charge on the photocatalyst. The influence of pH on the extent of photo-degradation of CPX (10 mg/L) was explored by altering the pH from 4 to 9 with 0.1 g/L of catalyst under solar illumination and the results are shown in **Figure 6**a. The percentage removal of CPX was found to be 69.7%, 63.6% and 66.8% at pH 4, pH 6 and pH 9 respectively. The maximum degradation efficiency for CPX over $Ag/Fe_2O_3/ZnO$ heterostructure was noted to be at pH 4, although the differences were not very large. CPX exists in a zwitterion form between pH values from 6.09-8.74, and CPX appeared to be slightly more sensitive under basic conditions. According to the pharmaceutical point of view, stability in acidic conditions is imperative because the formulation and use of oral pharmaceutical drugs is carried out in the range of pH 3.5 to 5.5 [98].The point of zero charge (PZC) for $Ag/Fe_2O_3/ZnO$ was calculated to be 3.78 (**Figure 6**b). At pH< 3.78, the surface of $Ag/Fe_2O_3/ZnO$ turned positively charged and negatively charged at pH > 3.78. At pH 4, CPX carries a net positive charge and $Ag/Fe_2O_3/ZnO$ behaves in an anionic way, which results in electrostatic attraction between them, thereby increasing the efficiency of the photocatalytic reaction at this lower pH.

Figure 6c describes the impact of catalyst loading towards the decomposition of CPX at pH 4 and 10 mg/L of CPX concentration. It was noticed that the extent of decomposition was increased from 69.7% to 76.4% with the increment in catalyst loading from 0.1 g/L to 0.3 g/L. The decomposition efficiency then decreased to 68.4% with the increment in catalyst loading up to 0.4 g/L. Increasing the amount of catalyst decreases solution transparency, which decreases penetration of photons in the more turbid solution and thus decreases photocatalytic performance. The influence of initial CPX concentration (**Figure 6**d) on degradation efficiency was also examined at pH 4 and a catalyst loading of 0.3 g/L. The extent of decomposition decreased with the rise in CPX initial concentration in the sequence: 84.6% >76.4 % > 68.0%.However, beyond the optimum drug concentration, the degradation efficiency decreases because of reduced availability of active sites for the higher drug concentrations.

It is well known that the inorganic salts are present in actual wastewater and many researchers reported the significant impact of inorganic salts on photocatalytic removal efficiency of the target contaminants [99]. Therefore, taking this factor into account, the impact of different inorganic salts (NO_3^-, CO_3^{2-}, SO_4^{2-}) in water on the photocatalytic degradation of CPX using $Ag/Fe_2O_3/ZnO$ heterostructure was studied. **Figure 6**e exhibits the results of CPX degradation in the presence of inorganic salts at a concentration of 0.02 M. As shown in Fig.

6e, no obvious difference was observed in the degradation curves of the solution containing $NaNO_3$ and Na_2SO_4.The photocatalytic efficiency for CPX declined to some extend with the introduction of Na_2CO_3. The reason for this may be that carbonate can also act as a radical scavenger, which can decompose some active radicals formed at the surface of photocatalyst, resulting in reduction of active radicals to combine with the CPX molecules, so that the photocatalytic degradation of CPX was impeded significantly. Similar results were reported in literature on the photocatalytic degradation of CPX by Wen *et al.* [100].

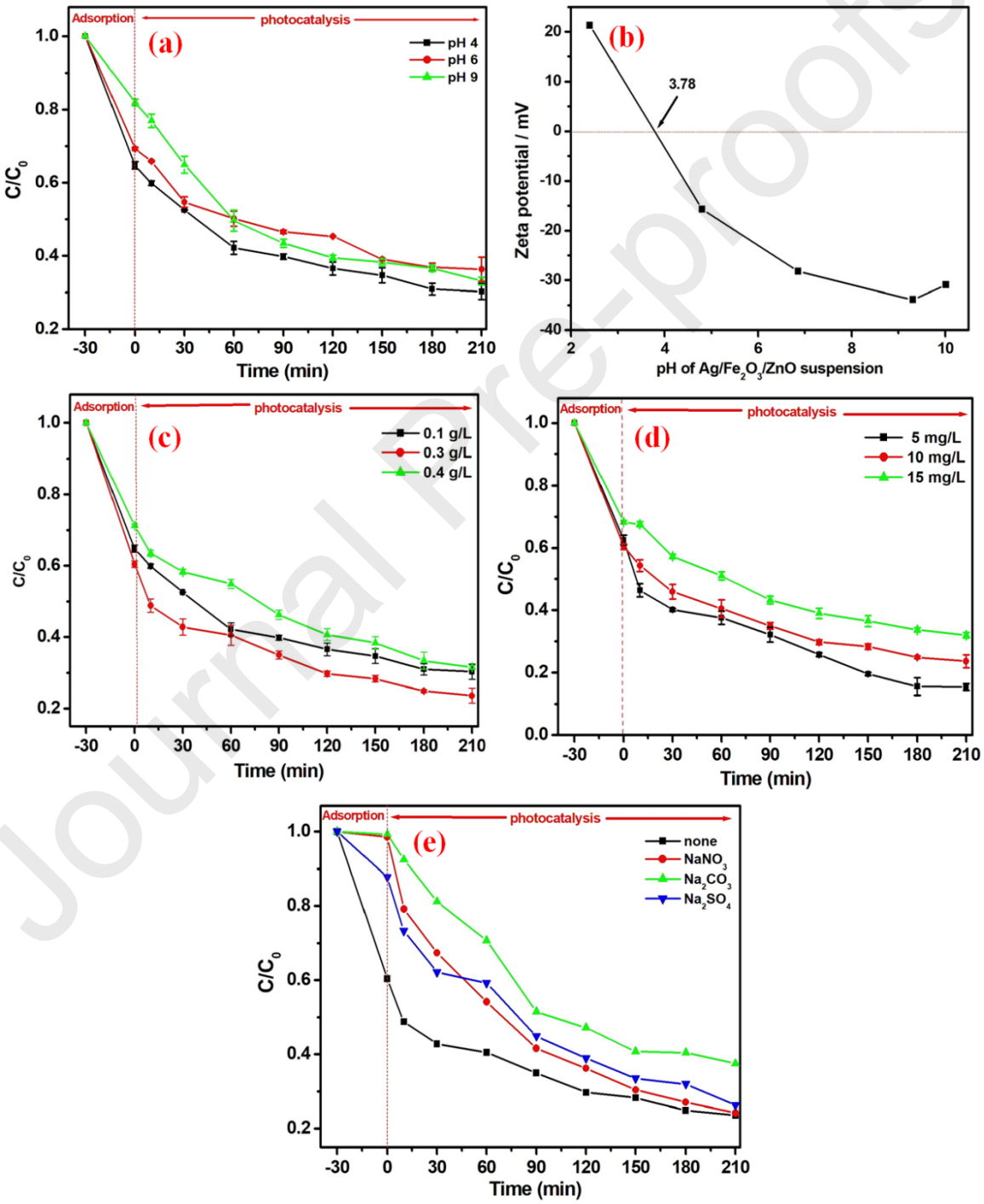

Figure 6. Effect of (a) pH (b) pH on zeta potential (c) catalyst amount and (d) initial CPX concentration on the removal efficiency of CPX under solar light using $Ag/Fe_2O_3/ZnO$ heterostructure (error bars based on repeated experiments) and (e) Effect of inorganic salts on CPX degradation in the presence of $Ag/Fe_2O_3/ZnO$ heterostructure.

The UV-vis absorbance spectra for the decomposition of CPX with respect to time over the $Ag/Fe_2O_3/ZnO$ heterostructure under solar light are illustrated in **Figure 7**a. The characteristic peak of CPX at 271 nm decreased progressively with the increase in photocatalytic reaction time. About 76.4% decomposition of CPX was accomplished over the $Ag/Fe_2O_3/ZnO$ heterostructure after 210 minutes of reaction. Furthermore, adsorption and photolysis studies were carried out to determine the impact of solar light and catalyst on CPX disappearance. It was found that about 33.1% of CPX was adsorbed on the surface of $Ag/Fe_2O_3/ZnO$ heterostructure. During a photolytic process in the absence of the heterostructure material, only 11% decomposition of CPX was attained after 210 minutes of solar illumination (**Figure 7**b). Moreover, only 43.2%, 63.1%, 28.2% and 64.5% of CPX was degraded over pristine Fe_2O_3, ZnO, Ag/Fe_2O_3 and Ag/ZnO respectively, under solar light which demonstrated lower decomposition efficiency as compared to the $Ag/Fe_2O_3/ZnO$ heterostructure (**Figure 7**c). Di *et al.* [101] synthesized nitrogen-doped carbon quantum dots (N-CQDs)/BiOBr using solvothermal method and utilized for the photocatalytic degradation of CPX (10 mg/L, 100 mL). The degradation efficiency of 88% was obtained after 120 minutes of visible illumination. In another study, N-CQDs/$BiPO_4$ composite showed maximum removal of CPX (10 mg/L) *i.e.* 87.5% as compared to bare $BiPO_4$ (64.4%) after 120 minutes of UV illumination [102]. This enhancement in degradation efficiency of CPX was due to the generation of more $O_2^{\bullet-}$ species with N-CQDs/$BiPO_4$ photocatalytic system.

The mineralization of CPX (pH 4, 10 mg/L) was analyzed using TOC analysis and photocatalytic experiments were performed under optimized conditions. The initial TOC concentration of CPX was obtained as 7.355 mg/L which reduced to 5.371 mg/L after 210 minutes of photocatalytic reaction. About 27% TOC reduction of CPX (10 mg/L, pH 4) was obtained with $Ag/Fe_2O_3/ZnO$ composite (0.3 g/L) after 210 minutes of solar illumination. It was found that the TOC values reduced with increase in reaction time.

The kinetics of the decomposition reaction was studied by application of a pseudo-first order kinetic model [103]. The plot of $\ln C_0/C$ versus reaction time (**Figure 7**d) suggested that the photocatalytic decomposition of CPX followed a pseudo-1st–order model, and the values

of the apparent rate constants are shown in **Table 1**. The rate constant for the $Ag/Fe_2O_3/ZnO$ heterostructure was found to be 5 times higher than that of bare Fe_2O_3.

Table 1: Apparent photocatalytic rate constants for three photocatalysts, and correlation coefficient for pseudo-first order model fit.

Photocatalyst	**R^2**	**Apparent rate constant (hr^{-1})**
$Ag/Fe_2O_3/ZnO$	0.98326	0.3036
Fe_2O_3	0.96979	0.0596
ZnO	0.97618	0.2802

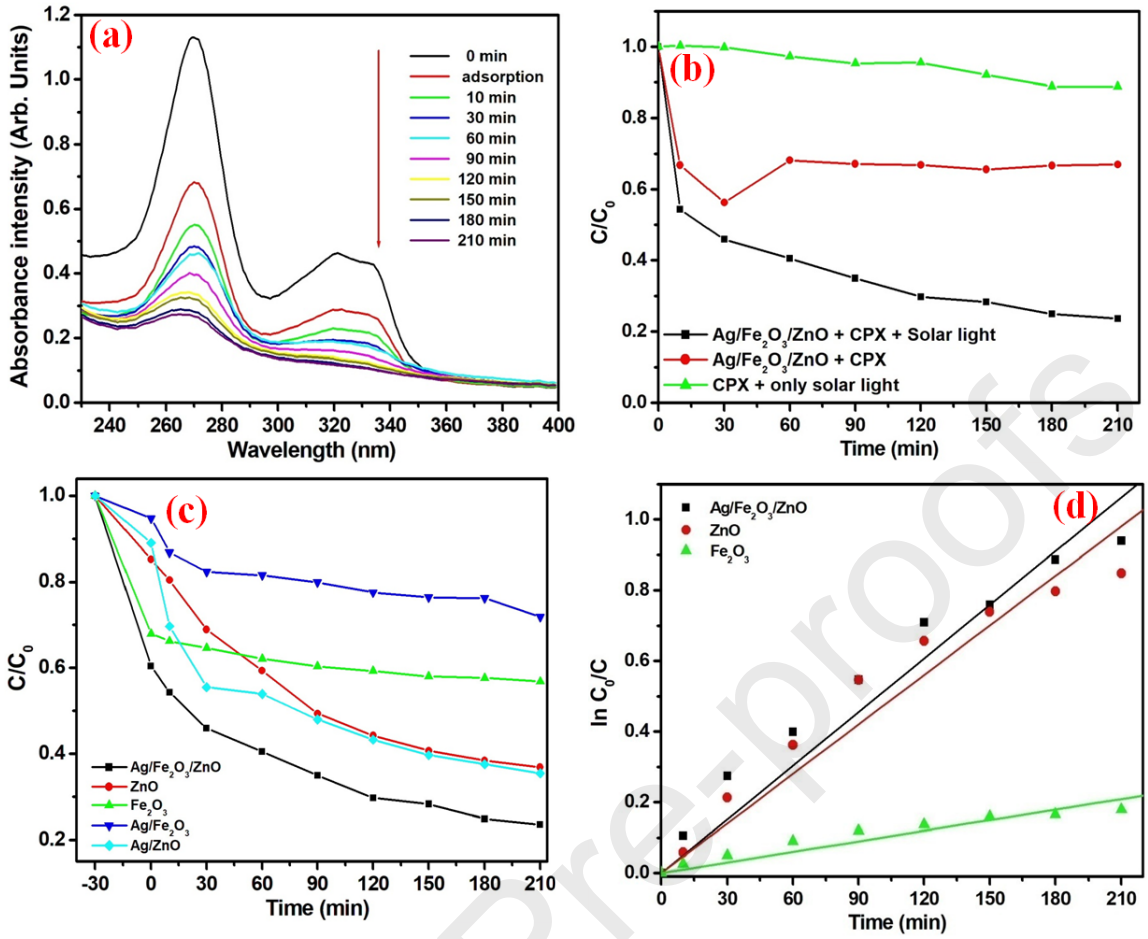

Figure 7. (a) Time dependent UV-visible absorbance spectra of CPX in the presence of $Ag/Fe_2O_3/ZnO$ heterostructure under optimized conditions (pH 4, catalyst loading 0.3 g/L, initial CPX concentration 10 mg/L), (b) comparison between photolysis, adsorption and photocatalysis with bare ZnO, Fe_2O_3, Ag/Fe_2O_3, Ag/ZnO and $Ag/Fe_2O_3/ZnO$ heterostructure (c) comparison of extent of degradation of CPX using bare Fe_2O_3, bare ZnO and $Ag/Fe_2O_3/ZnO$ heterostructure under solar illumination.

3.3 Scavenger study and probable mechanism for the decomposition of CPX using $Ag/Fe_2O_3/ZnO$ heterostructure

In order to study the degradation mechanism, role of reactive oxidative species in decomposition reaction was identified using different scavenging agents under the optimized reaction conditions. The decomposition efficiency of CPX (**Figure 8**a) was determined to be 45.5%, 19.5% and 47.3% for TEOA, FA and *p*-BQ, respectively. It was observed that the decomposition efficiency of CPX considerably decreased with the addition of FA (formic acid), suggesting that electrons are the foremost reactive species for the removal of CPX. It was noted that the decomposition efficiency of CPX diminished to 45.5% and 47.3% with TEOA and BQ,

respectively, suggesting that holes (h^+) and superoxide ($^{\bullet}O_2^-$) are also engaged in the decomposition of CPX to some extent. The non-fluorescent terephthalic acid (TA) directly combines with $^{\bullet}OH$ to generate the highly fluorescent 2-hydroxy terephthalic acid (HTA) which has maximum fluorescence emission intensity around 427 nm [104]. Therefore, the analysis of $^{\bullet}OH$ radical formation was analyzed using this TA probe method (**Figure 8**b). The enhancement in peak intensity at 427 nm with the increase in reaction time under solar light signified the formation of $^{\bullet}OH$ radicals. Hence, it was inferred that $^{\bullet}OH$ radicals, electrons, holes and reactive oxygen species played an important function towards the decomposition of CPX using $Ag/Fe_2O_3/ZnO$ heterostructure.

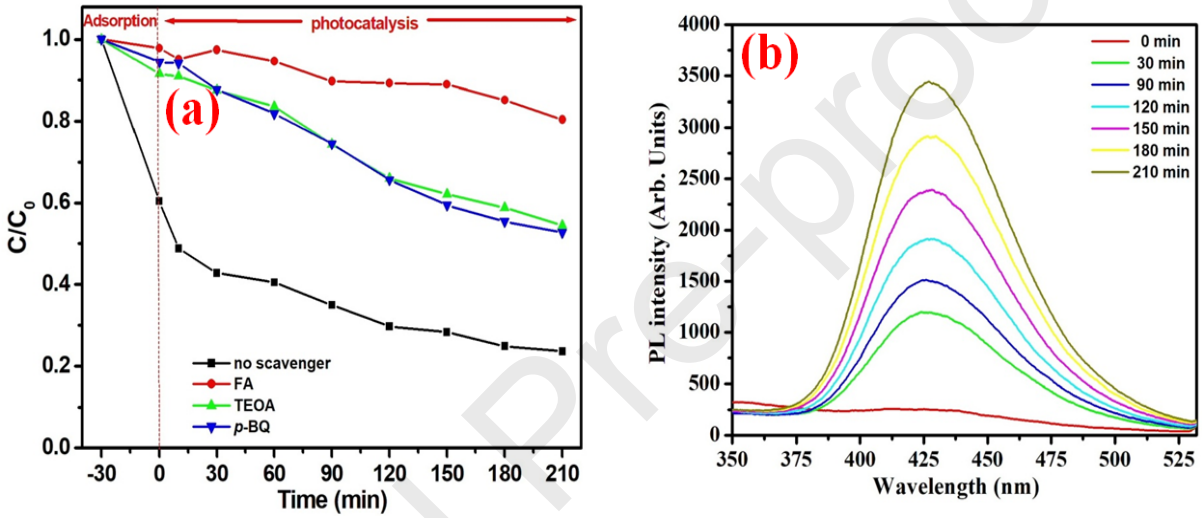

Figure 8. (a) Photocatalytic decomposition of CPX over $Ag/Fe_2O_3/ZnO$ heterostructure in presence of distinct scavengers and (b) Photoluminescence emission spectra of TA over $Ag/Fe_2O_3/ZnO$ heterostructure under solar illumination

To understand the energy band structure of the $Ag/Fe_2O_3/ZnO$ heterostructure, the actual energy band potentials of ZnO nanosheets and Fe_2O_3 nanorods were determined using valence band ultraviolet photoelectron spectroscopy (VB-UPS) and results are shown in Figure 9.

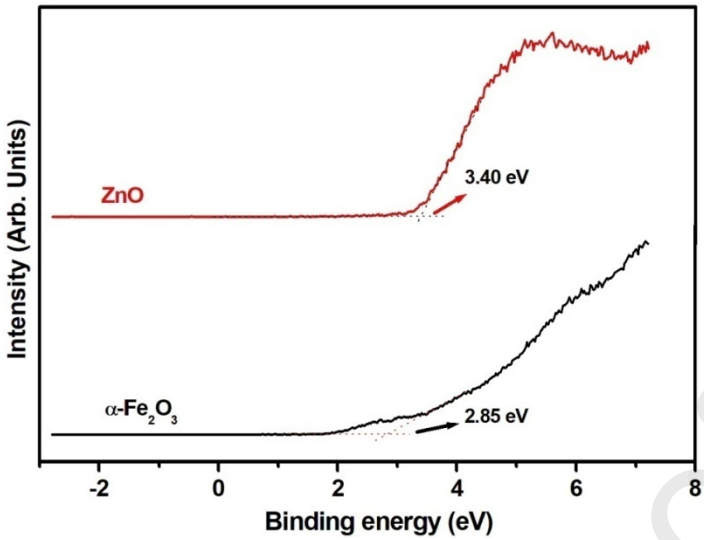

Figure 9 UPS spectra of ZnO nanoplates and α-Fe_2O_3 nanorods

The valence band maximum (E_{VB}) was determined to be 3.40 eV and 2.85 eV for ZnO and Fe_2O_3, respectively. The band gap energies (E_g) of ZnO and Fe_2O_3 were acquired from Tauc plot and found to be 3.18 and 2.07 eV, respectively. The conduction band minimum (E_{CB}) was found to be 0.22 eV and 0.78 eV for ZnO and Fe_2O_3, respectively using the relation [105-107], $E_{CB} = E_{VB} - E_g$. **Figure 10** exhibits a graphical depiction of the photocatalytic decomposition process using the Ag/Fe_2O_3/ZnO heterostructure. Under solar illumination, both Fe_2O_3 and ZnO could be stimulated to produce e^-/h+ pairs. Since the conduction band edge of Fe_2O_3 (0.78 eV) is more positive than ZnO (0.22 eV), the photo-excited e^- of ZnO can transfer from the conduction band of ZnO to Fe_2O_3. The photo-induced e^- from the conduction edge of ZnO can be trapped by Ag nanoparticles because of its high conductivity and electron trapping capacity [108]. This could help in decreasing the e^--h^+ recombination of charge carriers by improving charge separation. The electrons in Ag nanoparticles could be entrapped by an oxygen molecule (O_2) to form superoxide anions ($^{\bullet}O_2^-$), which further react with CPX [109]. In reverse, the h^+ may be transferred from the valance band of ZnO to Fe_2O_3. The h^+ on the valence band of Fe_2O_3 and the Ag nanoparticles could be used for the decomposition of CPX [110, 111]. Meanwhile, the h^+ may combine with water to form hydroxyl radicals because the valence band potential of Fe_2O_3 (2.85 eV) is higher than the standard potential of $^-OH/^{\bullet}OH$ (1.99 eV) [112]. As a result, e^-, h^+, $^{\bullet}O_2^-$, and $^{\bullet}OH$ play an important function towards the decomposition of CPX using Ag/Fe_2O_3/ZnO heterostructures under solar irradiation as also verified from the reactive species results. Therefore, the photocatalytic activity of the Ag/Fe_2O_3/ZnO heterostructure is noticeably improved over that of the ZnO and Fe_2O_3 components.

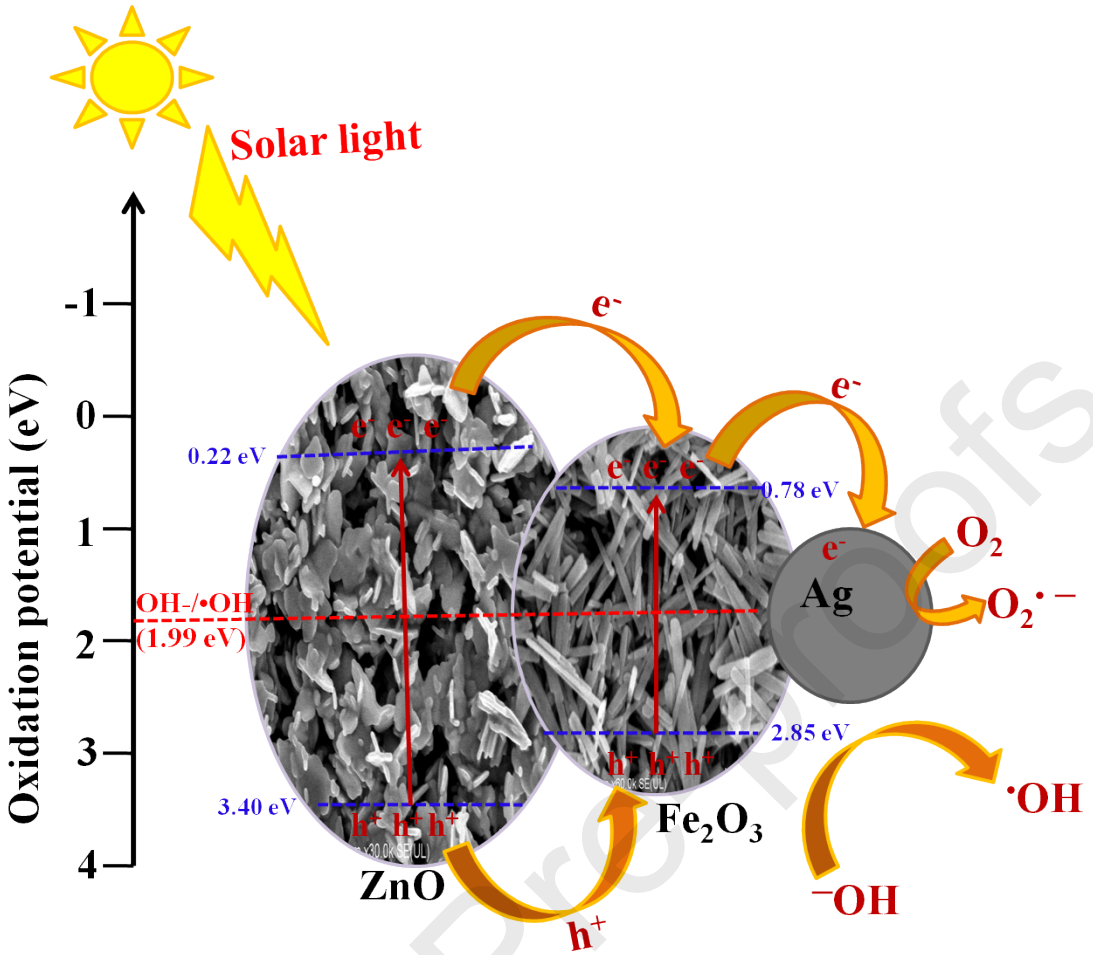

Figure 10 Pictorial illustration of the mechanism for the photocatalytic degradation over the $Ag/Fe_2O_3/ZnO$ heterostructure under solar illumination

3.4 Transformation products and CPX degradation pathway

To study the decomposition intermediates during the photocatalytic reaction, LCMS analysis was carried out. In this study, the transformation products and structural information of the antibiotic drug CPX was found based on the molecular ion peaks $[M+H]^+$. The parent ion peak of CPX emerged at m/z 332 with the molecular formula ($C_{17}H_{18}FN_3O_3$) and molecular weight (M = 331.13 g/mol). The related mass spectra of drug solutions after photocatalytic reaction of various time periods are presented in supplementary information (Figure S1). Based on the MS data findings, a probable degradation pathway (Scheme 1) was proposed. Defluorinated product CPX 1 (m/z 330) is mainly formed after the substitution of an OH group in place of the fluorine [113-115]. The formation of the intermediate (m/z 362) can be due to the stepwise decomposition of the piperazine side chain opening by an •OH group, which is also in accordance with the oxidation capacity of the functional groups. The intermediate

product with m/z 334 could be formed from m/z 362 by losing one aldehyde group [116]. The elimination of a second formaldehyde group from the piperazine substituent (m/z 334) would result in the formation of product CPX 3 (m/z 306) or generate CPX 2 with m/z 316 *via* defluorination. The products CPX 2 and CPX 3 can be further defluorinated to generate product CPX 4 (m/z 288) [117].

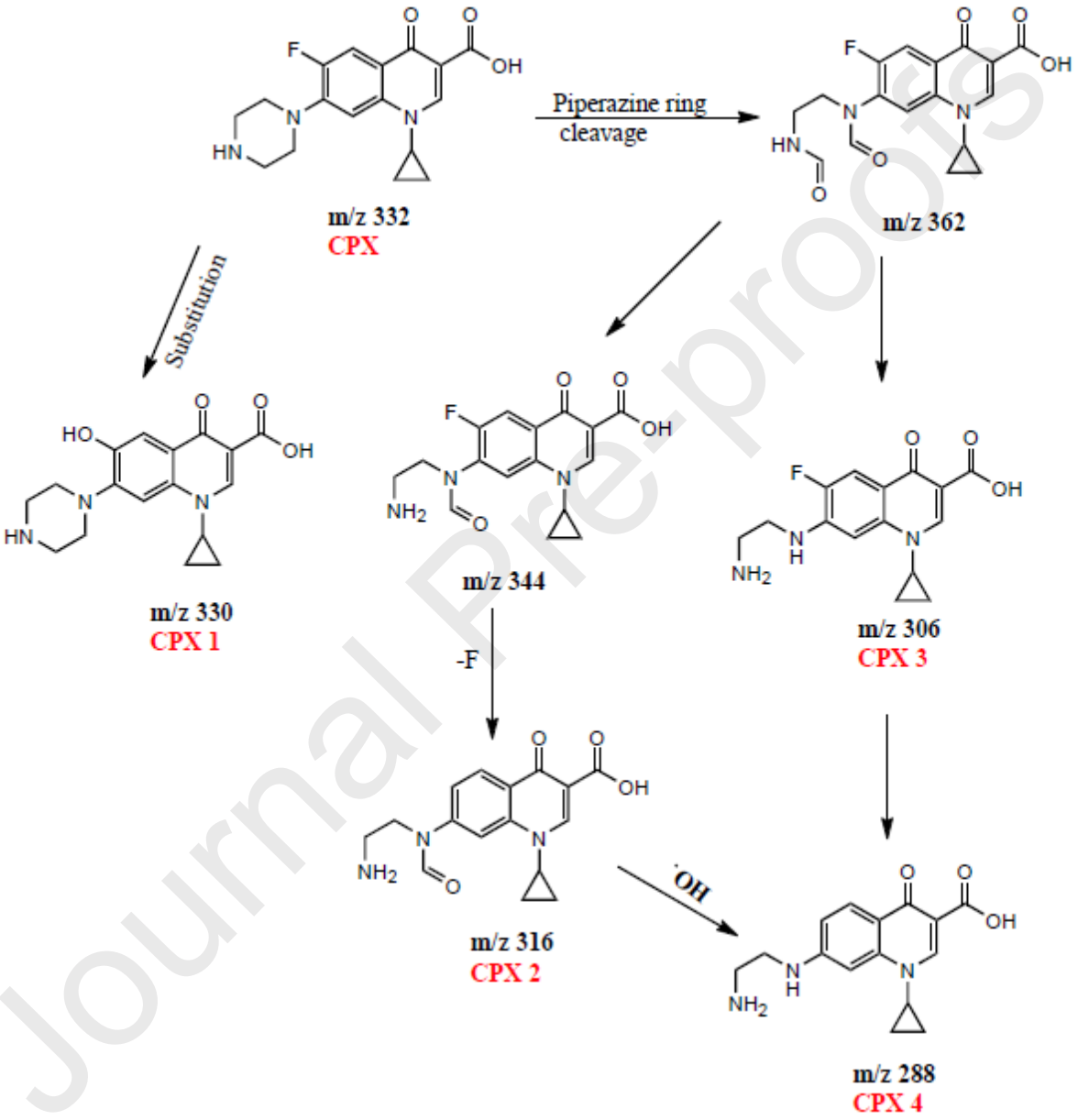

Scheme 1 Probable degradation pathway for the decomposition of CPX over Ag/Fe_2O_3/ZnO heterostructure under solar illumination

3.5 Reusability of prepared Ag/Fe_2O_3/ZnO heterostructure

To investigate the potential for a real application, CPX decomposition was studied over the Ag/Fe_2O_3/ZnO heterostructure for three continual cycles (**Figure 11**). The removal efficiency of CPX was slightly decreased as the number of runs increased. After two and three repeated runs, the CPX removal decreased from 76.4 % to 73.9 % and 64.2 %, respectively. The minor reduction in catalytic activity might be due to the leaching of zinc and silver ions and the loss of active sites during the degradation process. The prepared heterostructure exhibited reasonable catalytic stability and relatively small decreases in catalytic activity for CPX decomposition. Hence, the Ag/Fe_2O_3/ZnO heterostructure shows promise as a stable and efficient photocatalyst, which may be beneficial for realistic applications in the future, although more extensive stability studies are required.

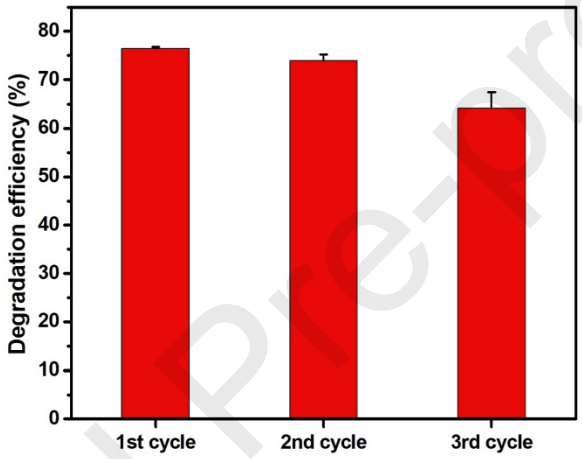

Figure 11 Recyclability of the Ag/Fe_2O_3/ZnO towards the decomposition of CPX under solar illumination over three cycles

3.6 Antibacterial activity of Ag/Fe_2O_3/ZnO heterostructure towards E.coli

3.6.1 Effect of exposure time

The impact of irradiation time on the antibacterial activity of the Ag/Fe_2O_3/ZnO heterostructure was studied by varying the exposure time under visible light for 30, 60 and 120 minutes. In **Figure 12**a, survival of bacterial in the absence of Ag/Fe_2O_3/ZnO heterostructure was used as control. Negligible photo-deactivation of *E. coli* was observed under visible light only. **Figure 12**a exhibits the photo-inhibition profile against *E. coli* catalyzed by the Ag/Fe_2O_3/ZnO heterostructure under visible illumination. The inhibition of *E. coli* increased with an increase in irradiation time. Almost complete (>90%) inactivation of *E. coli* was observed with 18.75 µg/mL and 2.34 µg/mL concentrations of Ag/Fe_2O_3/ZnO heterostructure after 60 minutes (optimized time) and 120 minutes of visible illumination (fluorescent lamps),

respectively. For comparison (**Figure 12**b), antibacterial experiments were carried out with the $Ag/Fe_2O_3/ZnO$ heterostructure sample under dark environments, where *E. coli* survival decreased slowly with time. There was a noticeable difference between the photo-induced and non-irradiated (dark) antibacterial effects against *E. coli* observed at a lower catalyst loading (0.01 -75 µg/mL) after 30 and 60 minutes of contact time. As seen from **Figure 12**, the prepared catalyst showed very good antimicrobial activity, as almost all *E.coli* was inactivated after 1 hour with a concentration of 18.75 µg/mL under visible illumination, whereas a concentration of 500 µg/mL was required for a similar antimicrobial effect under the dark conditions (**Figure 12**b). Since, both Zn and Ag are known for their antimicrobial properties. The chemical interactions between the metal ions and *E.coli* are a probable mechanism of $Ag/Fe_2O_3/ZnO$ against *E. coli* under dark conditions [118].

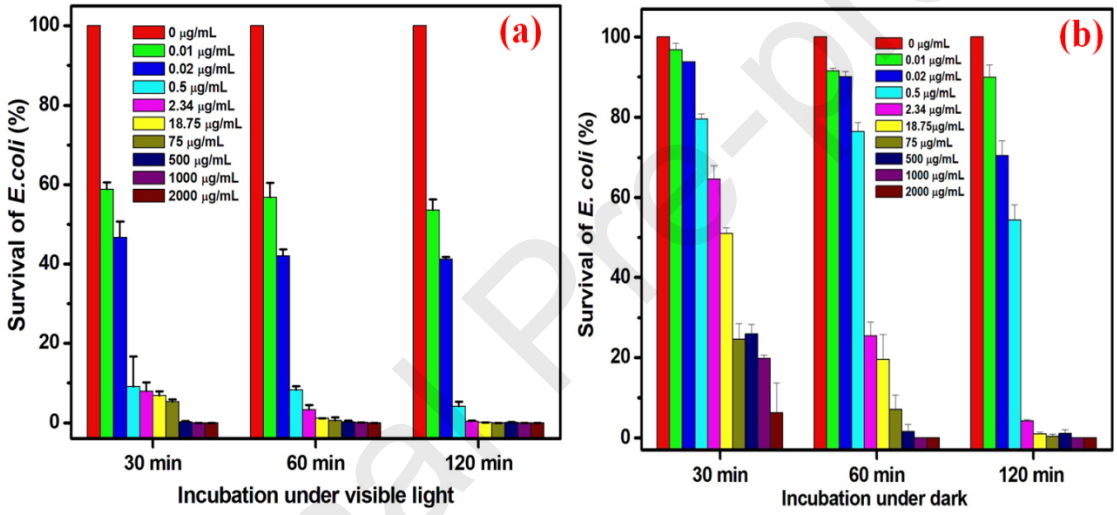

Figure 12. Percentage survival of *E. coli* after treatment with $Ag/Fe_2O_3/ZnO$at various concentrations as a function of time under (a) visible irradiation and (b) dark environment

3.6.2 Antimicrobial effect of $Ag/Fe_2O_3/ZnO$ loading

The impact of $Ag/Fe_2O_3/ZnO$ loading was explored by the incubation of *E. coli* (with a concentration of ~ 3×10^7 CFU/mL) for 60 minutes (optimized time) in the presence of different concentrations of $Ag/Fe_2O_3/ZnO$ (0-2000 µg/mL) under dark and visible light, with the outcomes quantified in **Figure 13**. The *E. coli* survival decreased with an increase in catalyst concentration under both conditions. The $Ag/Fe_2O_3/ZnO$ heterostructure (0.01 µg/mL) exhibited a minimal antibacterial activity (10%) towards *E. coli* in the dark, while 42% inactivation of *E. coli* was achieved after 60 minutes of visible illumination. On further increasing the catalyst loading to 18.75 µg/mL, almost complete photo-inactivation of *E. coli*

was achieved. On the other hand, 80% *E. coli* was deactivated under the dark conditions with the same high catalyst loading.

The greater deactivation of *E. coli* under visible illumination can be attributed to the generation of reactive oxygen species (ROS) on the surface of the $Ag/Fe_2O_3/ZnO$ heterostructure under visible illumination. As with the photocatalytic CPX degradation, the ROS were formed by the separation of e^- and h^+, whose functions were evaluated by the addition of chemical scavengers such glutathione (GSH) (a ROS scavenger for species such as $^{\bullet}OH$, H_2O_2, $O_2^{\bullet-}$) and EDTA (a scavenger for h^+) [119-121]. **Figure 13**c exhibits the plot of *E. coli* inactivation (%) in the presence of the two different scavengers. The extent of inactivation of *E. coli* decreased to 69.34% and 46.9% with the addition of GSH (0.05 mM) and EDTA (0.3 mM), respectively. The reduction in antibacterial activity confirms the role of $^{\bullet}OH$ and h^+ in bacterial inactivation under visible illumination. This can be expected, since Ag acts to capture electrons whereas holes decrease the hydroxyl ion on the surface of $Ag/Fe_2O_3/ZnO$ heterostructure to generate $^{\bullet}OH$ and further encourages the inhibition of bacteria [117, 122]. From **Figure 13**b, it can be noted that after 60 minutes of contact and overnight growth, the number of colonies of bacteria decreased with the increase in catalyst loading. On the other hand, the constant *E. coli* inactivation at higher catalyst loadings (**Figure 13**a) could be due to the screening effect causing a reduction in visible light reaching the photocatalysis and *E. coli* cell interface because of a higher concentration of $Ag/Fe_2O_3/ZnO$ particles in the aqueous medium [123].

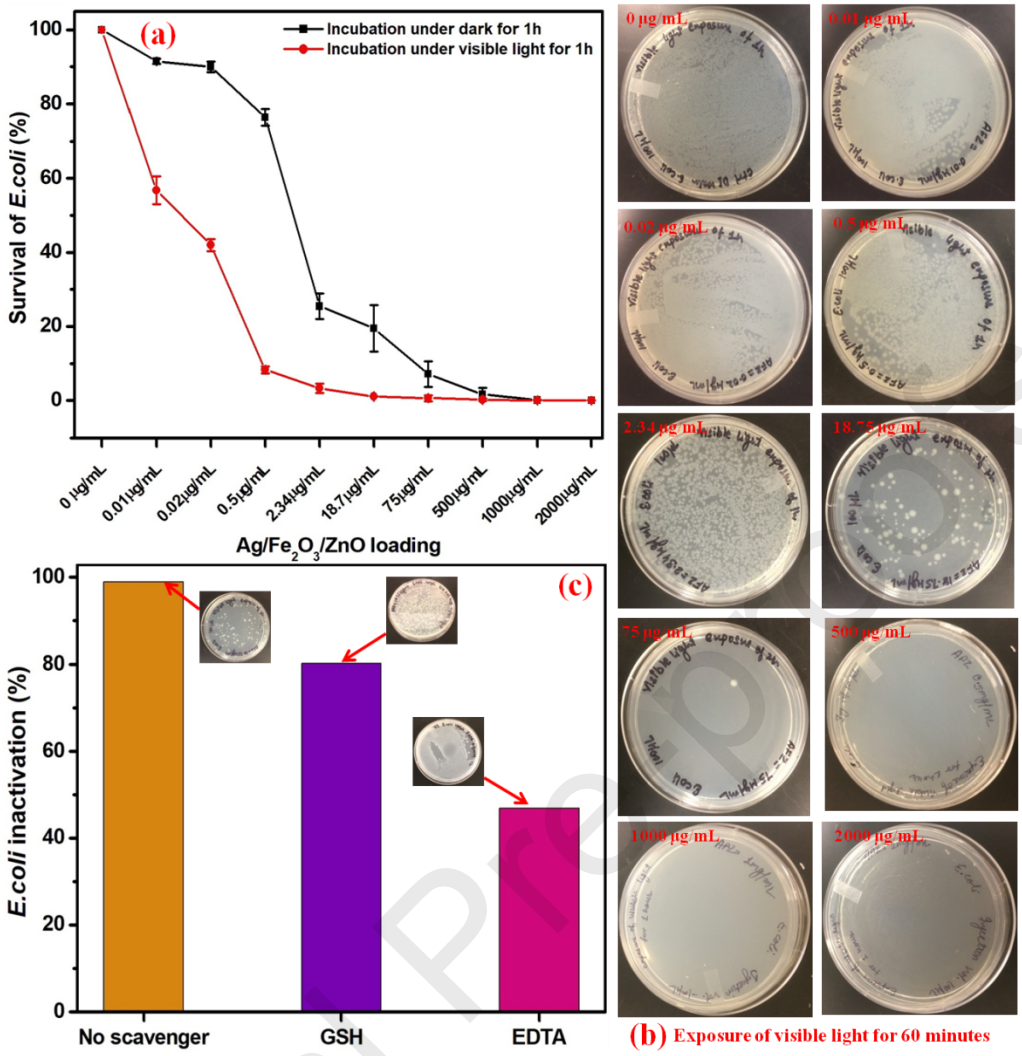

Figure 13 (a) Effect of $Ag/Fe_2O_3/ZnO$ loading on the *E. coli* inactivation under dark and visible light for 60 minutes, (b) Antibacterial activity of $Ag/Fe_2O_3/ZnO$ heterostructure evaluated for *E. coli* after 60 minutes of visible illumination. The concentrations of antibacterial agent are shown on the top of each plate at the same dilution, showing the growth of *E. coli* colonies (c) Photocatalytic inhibition efficiency against *E. coli* (3×10^7 CFU/mL) with different scavengers; GSH and EDTA in the presence of $Ag/Fe_2O_3/ZnO$ heterostructure under visible illumination.

In order to examine the nature of the antibacterial interactions, TEM imaging of the $Ag/Fe_2O_3/ZnO$ heterostructure treated *E. coli* was carried out. Generally, *E. coli* have a smooth surface with elliptical rod-shaped morphology [124]. From TEM images (**Figure 14**a and b), it was observed that the catalyst was attached to the *E. coli* surface and the bacteria showed some effects with the 18.34 μg/mL of $Ag/Fe_2O_3/ZnO$ after 30 minutes of contact time (**Figure 14**a and b). The prepared $Ag/Fe_2O_3/ZnO$ can apparently penetrate the wall of bacterial cell.

After 30 minutes, the centre portion of the *E. coli* was yet undamaged but the structure of wall seemed unclear, showing initial destruction to the cell wall (**Figure 14**b).

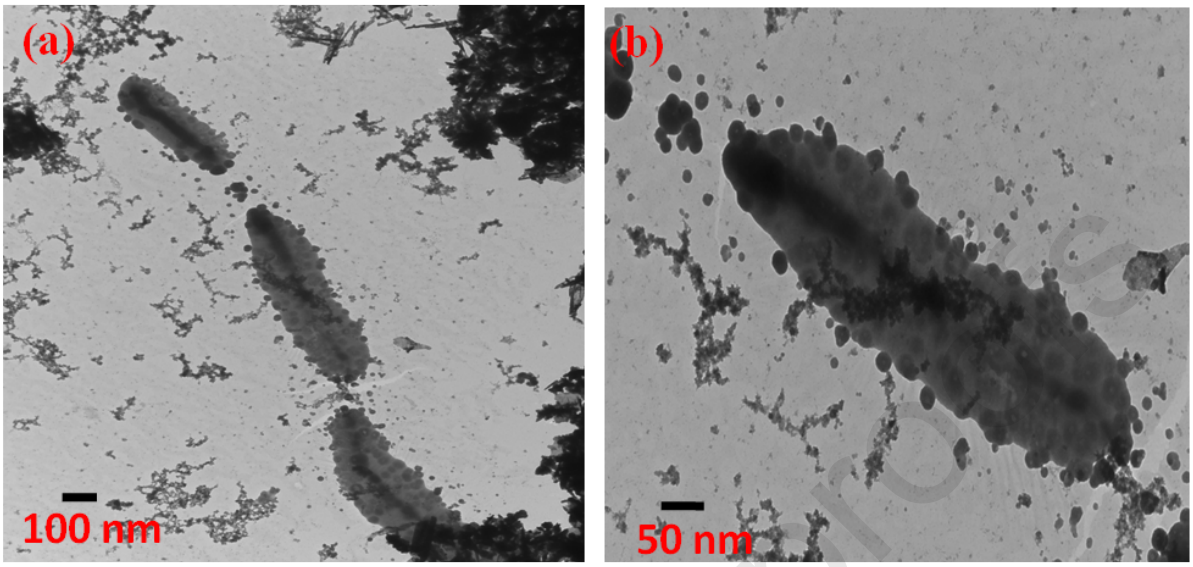

Figure 14. (a) TEM images of *E.coli* mixed with $Ag/Fe_2O_3/ZnO$ heterostructure (b) $Ag/Fe_2O_3/ZnO$ heterostructure anchored on the surface of *E. coli*

4. Conclusions

This study offered a new approach of fabricating ternary photocatalysts which were applied to pharmaceutical wastewater treatment and bacterial disinfection. $Ag/Fe_2O_3/ZnO$ heterostructure was successfully fabricated using a surfactant-free precipitation method and this was employed as a photocatalyst for the effective solar-light driven decomposition of CPX in aqueous phase. The materials characterization techniques confirmed the formation of the $Ag/Fe_2O_3/ZnO$ heterostructure. Morphological studies revealed that Ag nanoparticles are well dispersed on the surface of ZnO nanoplates and Fe_2O_3 nanorods. Further, the prepared heterostructure showed enhanced photocatalytic activity for CPX degradation (76.4%) compared to pristine Fe_2O_3 nanorods (43.2%), ZnO nanoplates (63.1%), Ag/Fe_2O_3 (28.2%) and Ag/ZnO (64.5%) under solar illumination. This superior photocatalytic performance can be due to the separation and transfer efficiency of charge carriers. Based on reactive species trapping experiments, a plausible photocatalytic mechanism and intermediate study for the decomposition of CPX was proposed. Preliminary recyclability experiments clearly exhibited the stability of the $Ag/Fe_2O_3/ZnO$ heterostructure for potential reuse. Antibacterial studies revealed that the $Ag/Fe_2O_3/ZnO$ heterostructure promoted faster *E. coli* deactivation under

visible light as compared to a dark environment. The generation of ROS species appears to be a key factor in the enhanced activity under visible light. Thus, $Ag/Fe_2O_3/ZnO$ can be potentially explored as a superb antibacterial agent and solar light responsive photocatalytic material in terms of environmental remediation.

Supporting Information

Mass spectrum data of parent compound and their intermediate products are given to support the presented results.

Conflicts of Interest

The authors declare no competing financial interest.

Acknowledgements

This study was supported by MODROB AICTE project (F. No. 9-181/RIFD/policy-1/2016-17) and TEQIP-III project grant of Dr. S.S. Bhatnagar University Institute of Chemical Engineering and Technology, Panjab University, Chandigarh. Amandeep Kaur would like to acknowledge CSIR, Government of India for awarding a fellowship under CSIR-SRF scheme (Grant No. 09/135/0750/2016-EMR-I) and Ministry of Human Resources Development (MHRD) and Shastri Institute for the honour of a fellowship under the SRFS-doctoral programme. A portion of this project was performed at the University of Waterloo, Canada, with the support of Prof. William A. Anderson. The authors would like to acknowledge the help of Ran An from the University of Waterloo for their assistance with TEM and Zeta analysis. The authors wish to appreciate SAIF, Panjab University, Chandigarh, NIPER, Mohali, IIT Ropar, and IIT Bombay, Mumbai for comprehensive characterization of prepared samples.

References

[1] Van-Doorslaer, X.; Dewuf, J.; Van-Langenhove, H.; Demeestere, K. Fluoroquinolone antibiotics: An emerging class of environmental micropollutants. *Sci. Total Environ.* **2014**, 500-501, 250-269.

[2] Khedr, T. M.; El-Sheikh, S. M.; Hakki, A.; Ismail, A. A.; Badawy, W. A.; Bahnemann, D. W. Highly active non-metals doped mixed-phase TiO_2 for

photocatalytic oxidation of ibuprofen under visible light. *J. Photochem. Photobiol., A* **2017**, 346, 530-540.

[3] Selvakumar, K.; Raja, A.; Arunpandian, M.; Stalindurai, K.; Rajasekaran, P.; Sami, P.; Nagarajan, E. R.; Swaminathan, M. Efficient photocatalytic degradation of ciprofloxacin and bisphenol a under visible light using Gd_2WO_6 loaded ZnO/bentonite nanocomposite. *Appl. Surf. Sci.* **2019**, 481, 1109-1119.

[4] Hassani, A.; Khataee, A.; Karaca, S.; Karaca, C.; Gholami, P. Ultrasound-assisted removal of acid red 17 using nanosized Fe_3O_4-loaded coffee waste hydrochar. *Ultrason. Sonochem.* **2017**, 35, 251-262.

[5] Kumar, J. V.; Karthik, R.; Chen, S.-M.; Muthuraj, V.; Karuppiah, C. Fabrication of potato-like silver molybdate microstructures for photocatalytic degradation of chronic toxicity ciprofloxacin and highly selective electrochemical detection of H_2O_2. *Sci. Rep.* **2016**, 6, 34149.

[6] Jallouli, N.; Pastrana-Martinez, L. M.; Ribeiro, A. R.; Moreira, N. F. F.; Faria, J. L. ; Hentati, O.; Silva, A. M. T.; Ksibi, M. Heterogeneous photocatalytic degradation of ibuprofen in ultrapure water, municipal and pharmaceutical industry wastewaters using a TiO_2/UV-LED system. *Chem. Eng. J.* **2018**, 334, 976-984.

[7] Santos, L.H.M.L.M.; Araujo, A.N.; Fachini, A.; Pena, A.; Delerue-Matos, C.; Montenegro, M. C. B. S. M. Ecotoxicological aspects related to the presence of pharmaceuticals in the aquatic environment. *J. Hazard. Mater.* **2010**, 175, 45-95.

[8] Sim, W. J.; Lee, J. W.; Lee, E. S.; Shin, S. K.; Hwang, S. R.; Oh, J. E. Occurrence and distribution of pharmaceuticals in wastewater from households, livestock farms, hospitals and pharmaceutical manufactures. *Chemosphere* **2011**, 82, 179-186.

[9] Feng, N.-X.; Yu, J.; Xiang, L.; Yu, L.Y.; Zhao, H. M.; Mo, C. H.; Li, Y.W.; Cai, Q. Y.; Wong, M. H.; Li, Q. X. Co-metabolic degradation of the antibiotic ciprofloxacin by the enriched bacterial consortium XG and its bacterial community composition. *Sci. Total Environ.* **2019**, 665, 41-51.

[10] Liu, Z.; Tian, J.; Zeng, D.; Yu, C.; Huang, W.; Yang, K.; Liu, X.; Liu, H. Binary-phase TiO_2 modified Bi_2MoO_6 crystal for effective removal of antibiotics under visible light illumination, *Mater. Res. Bull.* **2019**, 112, 336-345.

[11] Rakshit, S. S.; Sarkar, D.; Elzinga, E.; Punamiya, P.; Datta, R. Mechanisms of ciprofloxacin removal by nano-sized magnetite. *J. Hazard. Mater.* **2013**, 246–247, 221-226.

[12]Zaviska, F.; Drogui, P.; Grasmick, A.; Azais, A.; Héran, M. nanofiltration membrane bioreactor for removing pharmaceutical compounds. *J. Membr. Sci.* **2013**, 429, 121-129.

[13]Jiang, J. Q.; Zhou, Z.; Pahl, O. Preliminary study of ciprofloxacin (cip) removal by potassium ferrate (vi), *Sep. Purif. Technol.* **2012**, 88, 95-98.

[14]de Voogt P.; Janex-Habibi, Sacher, M. L., F.; Puijker, L.; Mons, M. Development of a common priority list of pharmaceuticals relevant for the water cycle, *Water Sci. Technol.* **2009**, 59, 39-46.

[15]Wang, X. H.; Lin, A.Y.C. Is the Phototransformation of pharmaceuticals a natural purification process that decreases ecological and human health risks? *Environ. Pollut.* **2014**, 186, 203-215.

[16]Fasugba, O.; Gardner, A.; Mitchell, B. G.; Mnatzaganian, G. Ciprofloxacin resistance in community- and hospital-acquired *Escherichia coli* urinary tract infections: a systematic review and meta-analysis of observational studies. *BMC Infect. Dis.* **2015**, 15, 545; doi: 10.1186/s12879-0151282-4.

[17]Venkatesan, A. K.; Halden, R. U. Wastewater treatment plants as chemical observatories to forecast ecological and human health risks of manmade chemicals. *Sci. Rep*. **2014**, 4, 3731.

[18]Chen, M.; Yao, J.; Huang, Y.; Gong, H.; Chu, W. Enhanced photocatalytic degradation of ciprofloxacin over $Bi_2O_3/(BiO)_2CO_3$ heterojunctions: efficiency, kinetics, pathways, mechanisms and toxicity evaluation, *Chem. Eng. J.* **2018**, 334, 453-461.

[19]Redgrave, L. S.; Sutton, S. B.; Webber, M. A.; Piddock, L. J. Fluoroquinolone resistance: mechanisms, impact on bacteria, and role in evolutionary success, *Trends Microbiol.* **2014**, 22, 438-445.

[20]Moussa, H.; Chouchene, B.; Gries, T.; Balan, L.; Mozet, K.; Medjahdi, G.; Schneider, R**.** Growth of zno nanorods on graphitic carbon nitride gCN sheets for the preparation of photocatalysts with high visible-light activity, *ChemCatChem* **2018**, 10, 4987-4997.

[21]Karthikeyan, S.; Kumar, S.; Durndell, L.; Isaacs, M.; Parlett, C.; Coulson, B.; Douthwaite, R.; Jiang, Z.; Wilson, K.; Lee, A. Size-dependent visible light photocatalytic performance of Cu_2O nanocubes. *ChemCatChem* **2018**, 10, 3554-3563.

[22] Di, J.; Xiong, J.; Li, H.; Liu, Z. Ultrathin 2D photocatalysts: electronic-structure tailoring, hybridization, and applications, *Adv. Mater.* **2018**, 30, 1704548.

[23] Ye, S.; Yan, M.; Tan, X.; Liang, J.; Zeng, G.; Wu, H.; Song, B.; Zhou, C.; Yang, Y.; Wang, H. Facile assembled biochar-based nanocomposite with improved graphitization for efficient photocatalytic activity driven by visible light, *Appl. Catal. B: Environ.* **2019**, 250, 78-88.

[24] Di, J.; Xia, J.; Chisholm, M. F.; Zhong, J.; Chen, C.; Cao, X.; Dong, F.; Chi, Z.; Chen, H.; Weng, Y.-X., Xiong, J.; Yang, S.-Z.; Li, H.; Liu, Z.; Dai, S. Defect-tailoring mediated electron–hole separation in single-unit-cell Bi_3O_4Br nanosheets for boosting photocatalytic hydrogen evolution and nitrogen fixation, *Adv. Mater.* **2019**, *31*, 1807576

[25] Lee, K. M.; Lai, C.W.; Ngai, K. S.; Juan, J. C. Recent developments of zinc oxide based photocatalyst in water treatment technology: a review, *Water Re*s. **2016**, 88, 428-448.

[26] Chong, M. N.; Jin, B.; Chow, C. W. K.; Saint, C. Recent developments in photocatalytic water treatment technology: a review, *Water Res.* **2010**, 44, 2997-3027.

[27] Mishra, M.; Chun, D. M. α-Fe_2O_3 as a photocatalytic material: a review. *Appl. Catal., A* **2015**, 498, 126-141.

[28] Duraimurugan, J.; Kumar, G.S.; Venkatesh, M.; Maadeswaran, P.; Girija, E. K. Morphology and size controlled synthesis of zinc oxide nanostructures and their optical properties, *J. Mater. Sci.: Mater. Electron.* **2018**, 29, 9339-9346.

[29] Moazzen, M. A. M.; Borghei, S. M.; Taleshi, F. Change in the morphology of zno nanoparticles upon changing the reactant concentration, *Appl. Nanosci.* **2013**, 3, 295-302.

[30] Wang, J.; Wang, Z.; Huang, B.; Ma, Y.; Liu, Y.; Qin, X.; Zhang, X.; Dai, Y. Oxygen vacancy induced band-gap narrowing and enhanced visible light photocatalytic activity of ZnO, *ACS Appl. Mater. Interfaces* **2012**, 4, 4024-4030.

[31] Rostami, M. Photodecomposition and adsorption of hazardous organic pollutants by Ce-doped ZnO@Ce-doped TiO_2-N/S-dual doped RGO ternary nano-composites photocatalyst for water remediation. *J. Mol. Struct.* **2019**, 1185, 191-199.

[32] Zhang, Y.; Gu, J.; Murugananthan, M.; Zhang, Y. Development of novel α-Fe_2O_3/$NiTiO_3$ heterojunction nanofibers material with enhanced visible-light photocatalytic performance. *J. Alloys Compd.* **2015**, 630, 110-116.

[33]Chen, L.; Wu, S.; Ma, D.; Shang, A.; Li, X. Optoelectronic modeling of the Si/α-Fe_2O_3 heterojunction photoanode. *Nano Energy* **2018**, 43, 177-183.

[34]Mendiola-Alvarez, S. Y.; Hernandez-Ramirez, A.; Guzman-Mar, J. L.; Maya-Trevino, M. L.; Caballero-Quintero, A.; Hinojosa-Reyes, L. A novel P-doped Fe_2O_3-TiO_2 mixed oxide: synthesis, characterization and photocatalytic activity under visible radiation. *Catal. Today* **2019**, 328, 91-98.

[35]Sen, T.; Shimpi, N. G.; Mishra, S.; Sharma, R. Polyaniline/γ-Fe_2O_3 nanocomposite for room temperature lpg sensing. *Sens. Actuators, B* **2014**, 190, 120-126

[36]Bhoi, Y. P.; Mishra, B. G. Single step combustion synthesis, characterization and photocatalytic application of α-Fe_2O_3-Bi_2S_3 heterojunctions for efficient and selective reduction of structurally diverse nitroarenes. *Chem. Eng. J.* **2017**, 316, 70-81.

[37]Xu, X.; Cao, R.; Jeong, S.; Cho, J. Spindle-like mesoporous α-Fe_2O_3 anode material prepared from MOF template for high-rate lithium batteries. *Nano Lett.* **2012**, 12, 4988-4991.

[38]Guo, R.; Qi, X.; Zhang, X.; Zhang, Z.; Cheng, X. Synthesis of Ag_2CO_3/α-Fe_2O_3 heterojunction and it high visible light driven photocatalytic activity for elimination of organic pollutants, *Sep. Purif. Technol.* **2019**, 211, 504-513.

[39]Formal, F. L.; Grätzel, M.; Sivula, K. Controlling photoactivity in ultrathin hematite films for solar water-splitting, *Adv. Funct. Mater.* **2010**, 20, 1099-1107.

[40]Li, L.; Koshizaki, N. Vertically aligned and ordered hematite hierarchical columnar arrays for applications in field-emission, superhydrophilicity, and photocatalysis, *J. Mater. Chem.* **2010**, 20, 2972-2978.

[41]Watermann, A.; Brieger, Mesoporous silica nanoparticles as drug delivery vehicles in cancer, *J. Nanomaterials* **2017**, 7, 189; doi:10.3390/nano7070189.

[42]Zhang, Z.; Liu, G.; Mao, Y. Improved separation efficiency of photogenerated carriers for fe_2o_3/$srtio_3$ heterojunction semiconductor. *Int. J. Hydrogen Energy* **2013**, 38, 9349-9354.

[43]Shooshtari, N. M.; Ghazi, M. M. an investigation of the photocatalytic activity of nano α-Fe_2O_3/ZnO on the photodegradation of cefixime trihydrate. *Chem. Eng. J.* **2017**, 315, 527-536.

[44]Xie, J.; Zhou, Z.; Lian, Y.; Hao, Y.; Li, P.; Wei, Y. Synthesis of α-Fe_2O_3/ZnO composites for photocatalytic degradation of pentachlorophenol under UV–vis light irradiation. *Ceram. Int.* **2015**, 41, 2622-2625.

[45] Yan, W.; Fan, H.; Yang, C. Ultra-fast synthesis and enhanced photocatalytic properties of alpha-Fe_2O_3/ZnO core-shell structure. *Mater. Lett.* **2011**, 65, 1595-1597.

[46] Xu, K.; Wu, J.; Tan, C. F.; Ho, G. W.; Wei, A.; Hong, M. Ag–CuO–ZnO metal–semiconductor multiconcentric nanotubes for achieving superior and perdurable photodegradation, *Nanoscale* **2017**, 9, 11574-11583.

[47] Liu, X.; Zhang, J.; Wang, L.; Yang, T.; Guo, X.; Wu, S.; Wang, S. 3D Hierarchically porous ZnO structures and their functionalization by au nanoparticles for gas sensors. *J. Mater. Chem.* **2011**, 21, 349-356.

[48] Zhu, P.; Chen, Y.; Duan, M.; Liu, M.; Zou, P.; Zhou, M. Enhanced visible photocatalytic activity of Fe-Cu-ZnO/graphene oxide photocatalysts for the degradation of organic dyes. *Can. J. Chem. Eng.* **2018**, 96, 1479-1488.

[49] Santillan-Urquiza, E.; Arteaga-Cardona, F.; Hernandez-Herman, E.; Pacheco-Garcia, P. F.; Gonzalez-Rodriguez, R.; Coffer, J. L.; Mendoza-Alvarez, M. E.; Velez-Ruiz, J. F.; Mendez-Rojas, M. A. Inulin as a novel biocompatible coating: evaluation of surface affinities toward $CaHPO_4$, α-Fe_2O_3, ZnO, $CaHPO_4$@ZnO and α-Fe_2O_3@ZnO nanoparticles. *J. Colloid Interface Sci.* **2015**, 460, 339-348.

[50] Mecha, A.C.; Onyango, M. S.; Ochieng, A.; Momba, M. N. B. Evaluation of synergy and bacterial regrowth in photocatalytic ozonation disinfection of municipal wastewater. *Sci. Total Environ.* **2017**, 601-602, 626-635.

[51] Ye, S.; Zeng, G.; Wu, H.; Zhang, C.; Liang, J.; Dai, J.; Liu, Z.; Xiong, W.; Wan, J.; Xu, P.; Cheng, M. Co-occurrence and interactions of pollutants, and their impact on soil remediation- a review. *Crit. Rev. Environ. Sci. Technol.* **2017**, 47, 1528-1553.

[52] Ye, S.; Zeng, G.; Wu, H.; Liang, J.; Zhang, C.; Dai, J.; Xiong, W.; Song, B.; Wu, S.; Yu, J. The effects of activated biochar addition on remediation efficiency of co-composting with contaminated wetland soil, Resour., *Conserv. Recycl.* **2019**, 140, 278-285.

[53] Wong, K.-A.; Lam, S. -M.; Sin, J.-C. Wet chemically synthesized ZnO structures for photodegradation of pre-treated palm oil mill effluent and antibacterial activity, *Ceram. Int.* **2019**, 45, 1868-1880.

[54] Guan, D. L.; Niu, C. G.; Wen, X. J.; Guo, H.; Deng, C. H.; Zeng, G. M. Enhanced *Escherichia coli* inactivation and oxytetracycline hydrochloride

degradation by a z-scheme silver iodide decorated bismuth vanadate nanocomposite under visible light irradiation. *J. Colloid Interface Sci.* **2018**, 512, 272-281.

[55]Jamil, T. S.; Mansor, E. S.; EI-Liethy, M. A. Photocatalytic Inactivation of *E. coli* using nano-size bismuth oxyiodide photocatalysts under visible light. *J. Environ. Chem. Eng.* **2015**, 3, 2463-2471.

[56]Sharma, N.; Jandaik, S.; Kumar, S.; Chitkara, M.; Sandhu, I. S. Synthesis, characterisation and antimicrobial activity of manganese- and iron-doped zinc oxide nanoparticles. *J. Exp. Nanosci.* **2016**, 11, 54-71.

[57] Ye, S.; Zeng, G.; Wu, H.; Zhang, C.; Dai, J.; Liang, J.; Yu, J.; Ren, X.; Yi, H.; Cheng, M.; Zhang, C. Biological technologies for the remediation of co-contaminated soil, *Crit. Rev. Biotechnol.* **2017**, 37, 1062-1076.

[58]Chong, M. N.; Cho, Y. J.; Poh, P. E.; Jin, B. Evaluation of titanium dioxide photocatalytic technology for the treatment of reactive black 5 dye in synthetic and real greywater effluents. *J. Cleaner Prod.* **2015**, 89, 196-202.

[59]Dutta, R. K.; Nenavathu, B. P.; Gangishetty, M. K.; Reddy, A. V. R. Studies on antibacterial activity of ZnO nanoparticles by ROS induced lipid peroxidation. *Colloids Surf., B Biointerfaces.* **2012**, 94, 143-150.

[60]Zhang, L.; Jiang, Y.; Ding, Y.; Daskalakis, N.; Jeuken, L.; Povey, M.; O'Neill, A. J.; York, D. W. Mechanistic investigation into antibacterial behaviour of suspensions of ZnO nanoparticles against *E. coli. J. Nanopart. Res.* **2010**, 12, 1625-1636.

[61]Ishiguro, H.;Nakano, R.;Yao, Y. Y.; Kajioka, J.S.; Fujishima, A.; Sunada, K.; Minoshima, M.; Hashimoto, K.; Kubota, Y. Photocatalytic inactivation of bacteriophages by TiO_2-coated glass plates under low-intensity, long-wavelength UV irradiation. Photochem. Photobiol. Sci. **2011**, 10, 1825-1829.

[62]Basnet, P.; Larsen, G. K.; Jadeja, R. P.; Hung, Y.-C.; Zhao, Y. α-Fe_2O_3 nanocolumns and nanorods fabricated by electron beam evaporation for visible light photocatalytic and antimicrobial applications. *ACS Appl. Mater. Interfaces* **2013**, 5, 2085-2095.

[63]Tam, K. H.; Djurisic, A. B.; Chan, C. M. N.; Xi, Y. Y.; Tse, C. W.; Leung, Y. H.; Chan, W. K.; Leung, F. C. C.; Au, D. W. T. Antibacterial activity of ZnO nanorods prepared by a hydrothermal method. *Thin Solid Films* **2018**, 516, 6167-6174.

[64] Achouri, F.; Merlin, C.; Corbel, S.; Alem, H.; Mathieu, L.; Balan, L., Medjahdi, G.; Said, M. B.; Gurabi, A.; Schneider, R. ZnO Nanorods with High Photocatalytic and antibacterial activity under solar light irradiation. *Materials* **2018**, 11, 2158.

[65] Kansal, S. K.; Lamba, R.; Mehta, S. K.; Umar, A. Photocatalytic degradation of alizarin red S using simply synthesized ZnO nanoparticles, *Mater. Lett.* **2013**,106 (2013) 385-389.

[66] Kaur, A.; Ibhadon, A.O.; Kansal, S. K. Photocatalytic degradation of ketorolac tromethamine (KTC) using Ag-doped ZnO microplates, *J. Mater. Sci.* **2017**, 52, 5256-5267.

[67] Maji, S. K.; Mukherjee, N.; Mondal, A.; Adhikary, B. synthesis, characterization and photocatalytic activity of α-Fe_2O_3 nanoparticles. *Polyhedron* **2012**, 33, 145-149.

[68] Mohammadzadeh, A.; Ramezani, M.; Ghaedi, A. M. Synthesis and characterization of Fe_2O_3–ZnO–$ZnFe_2O_4$/carbon nanocomposite and its application to removal of bromophenol blue dye using ultrasonic assisted method: optimization by response surface methodology and genetic algorithm. *J. Taiwan Inst. Chem. Eng.* **2016**, 59, 275-284.

[69] Samari, F.; Salehipoor, H.; Eftekhar, E.; Yousefinejad, S. Low-temperature biosynthesis of silver nanoparticles using mango leaf extract: catalytic effect, antioxidant properties, anticancer activity and application for colorimetric sensing, *New J. Chem.* **2018**, 42, 15905-15916.

[70] Yu, Q.; Zhu, J.; Xu, Z.; Huang, X. Facile synthesis of α-Fe_2O_3@SnO_2 core–shell heterostructure nanotubes for high performance gas sensors. *Sens. Actuators, B* **2015**, 213, 27-34.

[71] Elhalil, A.; Elmoubarki, R.; Farnane, M.; Machrouhi, A.; Sadiq, M.; Mahjoubi, F. Z.; Qourzal, S.; Barka, N. Photocatalytic degradation of caffeine as a model pharmaceutical pollutant on mg doped ZnO-Al_2O_3 heterostructure. *Environ. Nanotechnol. Monit. Manage.* **2018**, 10, 63-72.

[72] Ravi, K.; Mohan, B. S.; Sree, G. S.; Raju, I. M.; Basavaiah, K.; Rao, B. V. ZnO/RGO nanocomposite *via* hydrothermal route for photocatalytic degradation of dyes in presence of visible light. *Int. J. Chem. Stud.* **2018**, 6, 20-26.

[73] Chithra, M. J.; Sathya, M.; Pushpanathan, K. Effect of pH on crystal size and photoluminescence property of ZnO nanoparticles prepared by chemical precipitation method, *Acta Metall. Sinica* **2015**, 28, 394-404.

[74]Kadam, A. N.; Bhopate, D.P.; Kondalkar, V. V.; Majhi, S. M.; Bathula, C.D.; Tran, A.-V.; Lee, S.-W.; Facile synthesis of Ag-ZnO core–shell nanostructures with enhanced photocatalytic activity. *J. Ind. Eng. Chem.* **2018**, 61, 78-86.

[75]Guo, H.-L.; Zhu, Q.; Wu, X.-L.; Jiang, Y.-F.; Xie, X.; Xu, A.-W. Oxygen deficient ZnO_{1-x} nanosheets with high visible light photocatalytic activity. *Nanoscale* **2015**, 7, 7216-7223.

[76]Xu, L.; Xia, J.; Wang, K.; Wang, L.; Li, H.; Xu, H.; Huang, L.; He, M. Ionic liquid assisted synthesis and photocatalytic properties of α-Fe_2O_3 hollow microspheres, *Dalton Trans.* **2013**, 42, 6468-6477.

[77]Radzimska, A. K.; Markiewicz, E.; Jesionowski, T. Structural characterisation of ZnO particles obtained by the emulsion precipitation method. *J. Nanomater.* **2012**, 2012 Article ID 656353, 9 pages; https://doi.org/10.1155/2012/656353.

[78]Li, N.; Tian, Y.; Zhao, J.; Zhang, J.; Zhang, J.; Zuo, W.; Ding, Y. Efficient removal of chromium from water by Mn_3O_4@ZnO/Mn_3O_4 composite under simulated sunlight irradiation: synergy of photocatalytic reduction and adsorption, *Appl. Catal., B*, **2017**, 214, 126-136.

[79]Khalil, M. I.; Al-Qunaibit, M. M.; Al-Zahem, A. M.; Labis, J. P. Synthesis and characterization of ZnO nanoparticles by thermal decomposition of a curcumin zinc complex. *Arabian J. Chem.* **2014**, 7, 1178-1184.

[80]Li, X.; Lin, H.; Chen, X.; Niu, H.; Liu, J.; Zhang, T.; Qu, F. Dendritic α-Fe_2O_3/TiO_2 nanocomposites with improved visible light photocatalytic activity. *Phys. Chem. Chem. Phys.* **2016**, 18, 9176-9185.

[81]Han, L.; Wei, H.; Tu, B.; Zhao D. A facile one-pot synthesis of uniform core–shell silver nanoparticle @ mesoporous silica nanospheres. *Chem. Commun.* **2011**, 47, 8536-8538.

[82]Yu, M.; Liu, P.; Zhang, S.; Liu, J.; An, J.; Li, S. Preparation of graphene–Ag composites and their application for electrochemical detection of chloride. *Mater. Res. Bull.* **2012**, 47, 3206-3210.

[83]Hosseini-Sarvari, M.; Ataee-Kachouei, T.; Moeini, F. A novel and active catalyst Ag/ZnO for oxidant-free dehydrogenation of alcohols. *Mater. Res. Bull.* **2015**, 72, 98-105.

[84]Yang, C.; Li, Q. ZnO Inverse opals with deposited Ag nanoparticles: fabrication, characterization and photocatalytic activity under visible light irradiation. *J. Photochem. Photobiol., A* **2019**, 371, 118-127.

[85]Di, G.; Zhu, Z.; Zhang, H.; Zhu, J.; Qiu, Y.; Yin, D.; Kuppers, S. Visible-light degradation of sulfonamides by Z-scheme ZnO/g-C_3N_4 heterojunctions with amorphous Fe_2O_3 as electron mediator. *J. Colloid Interface Sci.* **2019**, 538, 256-266.

[86]Huang, H.; Liu, J.; Liu, X.; Xiao, J.; Zhong, S.; She, X.; Fu, Z.; Yin, D. Microwave-dried α-Fe_2O_3 as a highly efficient catalyst for ortho-methylation of phenol with methanol. *Fuel* **2016**, 182, 373-381.

[87]Liu, Y.; Yu, L.; Hu, Y.; Guo, C.; Zhang, F.; Lou, X. W. A Magnetically separable photocatalyst based on nest-like γ-Fe_2O_3/ZnO double-shelled hollow structures with enhanced photocatalytic activity. *Nanoscale* **2012**, 4, 183-187.

[88]Singh, P.; Sudhaik, A.; Raizada, P.; Shandilya, P.; Sharma, R.; Hosseini-Bandegharaei, A. Photocatalytic performance and quick recovery of BiOI/Fe_3O_4@graphene oxide ternary photocatalyst for photodegradation of 2,4-dintirophenol under visible light. Mater. *Today Chem.* **2019***,* 12, 85-95.

[89]Zhang, X.; Wang, Y.; Hou, F.; Li, H.; Yang, Y.; Zhang, X.; Yang, Y.; Wang, Y. Effects of Ag loading on structural and photocatalytic properties of flower-like ZnO microspheres. *Appl. Surf. Sci.* **2017**, 391, 476-483.

[90]Xu, B.; Li, Y.; Gao, Y.; Liu, S.; Lv D.; Zhao, S.; Gao, H.; Yang, G.; Li, N.; Ge, L. Ag-AgI/Bi_3O_4Cl for efficient visible light photocatalytic degradation of methyl orange: the surface plasmon resonance effect of Ag and mechanism insight, *Appl. Catal., B* **2019**, 246, 140-148.

[91]Zhao, Y.; Wang, Y.; Liang, X.; Shi, H.; Wang, C.; Fan, J.; Hu, X.; Liu, E. Enhanced photocatalytic activity of Ag-$CsPbBr_3$/CN composite for broad spectrum photocatalytic degradation of cephalosporin antibiotics 7-ACA, *Appl. Catal., B* **2019**, 247, 57-69.

[92]Kaur, M.; Umar, A.; Mehta, S. K.; Kansal, S. K. Reduced graphene oxide-CdS heterostructure: an efficient fluorescent probe for the sensing of Ag(I) and sunset yellow and a visible-light responsive photocatalyst for the degradation of levofloxacin drug in aqueous phase. *Appl. Catal., B* **2019**, 245, 143-158.

[93]Zhang, H.; Lv, X.; Li, Y.; Wang, Y.; Li, J. P25-graphene composite as a high performance photocatalyst, *ACS Nano* **2010**, 4, 380-386.

[94]Wang, S.; Kuang, P.; Cheng, B.; Yu, J.; Jiang, C. ZnO hierarchical microsphere for enhanced photocatalytic activity. *J. Alloys Compd.* **2018**, 741, 622-632.

[95]Li, B.; Yu, X.; Yu, X.; Du, R.; Liu, L.; Zhang, Y. Graphene quantum dots decorated ZnO-$ZnFe_2O_4$ nanocages and their visible light photocatalytic activity. *Appl. Surf. Sci.* **2019**, 478, 991-997.

[96]Shi, R.; Yang, P.; Song, X.; Wang, J.; Che, Q.; Zhang, A. ZnO flower: Self-assembly growth from nanosheets with exposed {1 1¯ 0 0} facet, white emission, and enhanced photocatalysis. *Appl. Surf. Sci.* **2016**, 366, 506-513.

[97]Hou, X.; Liu, J.; Guo, W.; Li, S.; Shi, Y.; Zhang, C. A Novel 3D-structured flower-like bismuth tungstate/mag-graphene nanoplates composite with excellent visible-light photocatalytic activity for ciprofloxacin degradation. *Catal. Commun.* **2019**,121, 27-31.

[98]EI-Kemary, M.; EI-Shamy, H.; EI-Mehasseb, I. Photocatalytic degradation of ciprofloxacin drug in water using ZnO nanoparticles. *J. Lumin.* **2010**, 130, 2327-2331.

[99]Tang, L. Wang, J.; Zeng, G.; Liu, Y.; Deng, Y.; Zhou, Y.; Tang, J.; Wang, J.; Guo, Z. Enhanced photocatalytic degradation of norfloxacin in aqueous Bi_2WO_6 dispersions containing nonionic surfactant under visible light irradiation, J. Hazard Mater. **2016**, 306, 295-304.

[100] Wen, X. J.; Niu, C. G.; Zhang, L.; Liang, C.; Guo, H.; Zeng, G. M. Photocatalytic degradation of ciprofloxacin by a novel Z-scheme CeO_2–Ag/AgBr photocatalyst: Influencing factors, possible degradation pathways, and mechanism insight, J. Catal. **2018**, 358, 141-154.

[101] Di, J.; Xia, J.; Ji. M.; Wang, B.; Li, X.; Zhang, Q.; Chen, Z.; Li, H. Nitrogen-doped carbon quantum dots/BiOBr ultrathin nanosheets: in situ strong coupling and improved molecular oxygen activation ability under visible light irradiation, ACS Sustainable Chem. Eng. **2016,** 4, 136-146.

[102] Di, J.; Xia, J.; Chen, X.; Ji, M.; Yin, S.; Zhang, Q.; Li, H. Tunable oxygen activation induced by oxygen defects in nitrogen doped carbon quantum dots for sustainable boosting photocatalysis, Carbon, **2017**, 114, 601-607.

[103] Liu, N.; Lu, N.; Su, Y.; Wang, P.; Quan, X. Fabrication of g-C_3N_4/Ti_3C_2 composite and its visible-light photocatalytic capability for ciprofloxacin degradation. *Sep. Purif. Technol.* **2019**, 211, 782-789.

[104] Lian, J.; Liu, P.; Li, X.; Bian, B.; Zhang, X.; Liu, Z.; Zhang, X.; Fan, G.; Gao, L.; Liu, Q. Multi-layer CeO_2-wrapped Ag_2S Microspheres with Enhanced

Peroxidase-like Activity for Sensitive Detection of Dopamine. *Colloids Surf., A*, **2019**, 565, 1-7.

[105] Di, J.; Chen, C.; Yang, S. Z.; Chen, S.; Duan, M.; Xiong, J.; Zhu, C.; Long, R.; Hao, W.; Chi, Z.; Chen, H.; Weng, Y.-X.; Xia, J.; Song, L.; Li, S.; Li. H.; Liu, Z. Isolated single atom cobalt in Bi_3O_4Br atomic layers to trigger efficient CO_2 photoreduction, Nature commun. **2019**, 10, 2840.

[106] Luo, Q.; Yang, X.; Zhao, X.; Wang, D.; Yin, R.; Li, X.; An, J. Facile preparation of well-dispersed ZnO/cyclized polyacrylonitrile nanocomposites with highly enhanced visible-light photocatalytic activity, *Appl. Catal. B: Environ.* **2017**, 204, 304-315.

[107] Wang, J. C.; Yao, H. C.; Fan, Z. Y.; Zhang, L.; Wang, J.-S.; Zang, S.-Q.; Li, Z. J. Indirect Z-Scheme BiOI/g-C_3N_4 photocatalysts with enhanced photoreduction CO_2 activity under visible light irradiation, *ACS Appl. Mater. Interfaces* **2016**, 8, 3765−3775.

[108] Arsana, P.; Bubpa, C.; Sang-aroon, W. Photocatalytic activity under solar irradiation of silver and copper doped zinc oxide: photodeposition versus liquid impregnation methods. *J. Appl. Sci.* **2012**, 12, 1809-1816.

[109] Liu, H.; Hu, C.; Zhai, H.; Yang, J.; Liu, X.; Jia, H. Fabrication of In_2O_3/ZnO@Ag nanowire ternary composites with enhanced visible light photocatalytic activity, *RSC Adv* **2017**, 7, 37220-37229.

[110] Xu, K.; Wu, J.; Tan, C. F.; Ho, G. W.; Wei, A.; Hong, M. Ag–CuO–ZnO metal–semiconductor multiconcentric nanotubes for achieving superior and perdurable photodegradation. *Nanoscale* **2017**, 9, 11574-11583.

[111] Saravanan, R.; Agarwal, S.; Gupta, V. K.; Khan, M. M.; Gracia, F.; Mosquera, E.; Narayanan, V.; Stephen, A. Line defect Ce^{3+} induced Ag/CeO_2/ZnO nanostructure for visible-light photocatalytic activity. *J. Photochem. Photobiol., A* **2018**, 353, 499-506.

[112] Wang, R.; Cao, L. Facile Synthesis of a novel visible-light-driven $AgVO_3$/$BiVO_4$ heterojunction photocatalyst and mechanism insight. *J. Alloys Compd.* **2017**, 722, 445-451.

[113] Paul, T.; Dodd, M. C.; Strathmann, T. J. Photolytic and photocatalytic decomposition of aqueous ciprofloxacin: transformation products and residual antibacterial activity. *Water Res.* **2010**, 44, 3121-3132.

[114] Lai, C.; Zhang, M.; Li, B.; Huang, D.; Zeng, G.; Qin, L.; Liu, X.; Yi, H.; Cheng, M.; Li, L.; Chen, Z.; Chen, L. Fabrication of CuS/$BiVO_4$ (0 4 0) binary heterojunction photocatalysts with enhanced photocatalytic activity for ciprofloxacin degradation and mechanism insight. *Chem. Eng. J.* **2019**, 358, 891-902.

[115] Wang, Y.; Shen, C.; Zhang, M.; Zhang, B.-T.; Yu, Y. -G. The electrochemical degradation of ciprofloxacin using a SnO_2-Sb/Ti anode: influencing factors, reaction pathways and energy demand. *Chem. Eng. J.* **2016**, 296, 79-89.

[116] Sayed, M.; Khan, J. A.; Shah, L. A.; Shah, N. S.; Shah, F.; Khan, H. M.; Zhang, P.; Arandiyan, H. solar light responsive poly(vinyl alcohol)-assisted hydrothermal synthesis of immobilized tio_2/ti film with the addition of peroxymonosulfate for photocatalytic degradation of ciprofloxacin in aqueous media: a mechanistic approach. *J. Phys. Chem. C* **2018**, 122, 406-421.

[117] Ji, Y.; Ferronato, C.; Salvador, A.; Yang, X.; Chovelon, J.-M. degradation of ciprofloxacin and sulfamethoxazole by ferrous-activated persulfate: implications for remediation of groundwater contaminated by antibiotics. *Sci. Total Environ.* **2014**, 472, 800-808.

[118] Jiang, Y.; Zhang, L.; Wen, D., Ding, Y. Role of physical and chemical interactions in the antibacterial behavior of ZnO nanoparticles against *E. coli. Mater. Sci. Eng. C* **2016**, 69, 1361-1366.

[119] Ogino, C.; Dadjour, M. F.; Takaki, K.; Shimizu, N. Enhancement of sonocatalytic cell lysis of *Escherichia coli* in the presence of TiO_2. *Biochem. Eng. J.* **2006**, 32, 100-105.

[120] Zhang, Y. N.; Duan, K. M. Glutathione exhibits antibacterial activity and increases tetracycline efficacy against pseudomonas aeruginosa. *Sci. China, Ser. C: Life Sci.* **2009**, 52, 501-505.

[121] Adhikari, S.; Banerjee, A.; Eswar, N. K. R.; Sarkar, D.; Madras, G. Photocatalytic inactivation of *E. Coli* by ZnO–Ag nanoparticles under solar radiation. *RSC Adv.* **2015**, 5, 51067-51077.

[122] Cai, Y.; Fan, H.; Xu, M.; Li, Q. Rapid photocatalytic activity and honeycomb Ag/ZnO heterostructures via solution combustion synthesis. *Colloids Surf., A* **2013**, 436, 787-795.

[123] Benabbou, A. K.; Derriche, Z.; Felix, C.; Lejeune, P.; Guillard, C. Photocatalytic inactivation of *Escherischia coli*: Effect of concentration of

TiO_2 and microorganism, nature, and intensity of UV irradiation. *Appl. Catal. B* **2007**, 76, 257-263.

[124] Xue, R.; Liu, Y.; Zhang, Q.; Liang, C.; Qin, H.; Liu, P.; Wang, K.; Zhang, X.; Chen, L.; Wei, Y. Shape changes and interaction mechanism of *Escherichia coli* cells treated with sericin and use of a sericin-based hydrogel for wound healing. *Appl. Environ. Microbiol.* **2016**, 82, 4663-4672.

Solar Light Active $Ag/Fe_2O_3/ZnO$ Heterostructure for Photodegradation of Ciprofloxacin, Transformation Products and Antibacterial Activity

Amandeep Kaur[1], William A. Anderson[2], Shazia Tanvir[2], Sushil Kumar Kansal[1]*

[1]Dr. S. S. Bhatnagar University Institute of Chemical Engineering and Technology, Panjab University, Chandigarh, 160014, India

[2]Department of Chemical Engineering, University of Waterloo, 200 University Avenue West, Waterloo, Ontario, N2L 3G1, Canada

Graphical abstract